The Astrophysical Journal, 694:718–733, 2009 April 1 doi:10.1088/0004-637X/694/2/718

IMAGING THE CIRCUMNUCLEAR REGION OF NGC 1365 WITH *CHANDRA*

Junfeng Wang[1], G. Fabbiano[1], M. Elvis[1], G. Risaliti[3], J. M. Mazzarella[2], J. H. Howell[2], and S. Lord[2]
[1] Harvard-Smithsonian Center for Astrophysics, 60 Garden St, Cambridge, MA 02138, USA; juwang@cfa.harvard.edu, pepi@cfa.harvard.edu, elvis@cfa.harvard.edu, risaliti@cfa.harvard.edu
[2] Infrared Processing and Analysis Center, California Institute of Technology, MS 100-22, Pasadena, CA 91125, USA; mazz@ipac.caltech.edu, jhhowell@ipac.caltech.edu, lord@ipac.caltech.edu
[3] Current Address: INAF-Arcetri Observatory, Largo E, Fermi 5, I-50125 Firenze, Italy.
Received 2008 September 25; accepted 2008 December 30; published 2009 March 19

ABSTRACT

We present the first *Chandra*/ACIS imaging study of the circumnuclear region of the nearby Seyfert galaxy NGC 1365. The X-ray emission is resolved into pointlike sources and complex, extended emission. The X-ray morphology of the extended emission shows a biconical soft X-ray-emission region extending ∼5 kpc in projection from the nucleus, coincident with the high-excitation outflow cones seen in optical emission lines particularly to the northwest. Harder X-ray emission is detected from a kpc-diameter circumnuclear ring, coincident with the star-forming ring prominent in the *Spitzer* mid-infrared (IR) images; this X-ray emission is partially obscured by the central dust lane of NGC 1365. Spectral fitting of spatially separated components indicates a thermal plasma origin for the soft extended X-ray emission ($kT = 0.57$ keV). Only a small amount of this emission can be due to photoionization by the nuclear source. Detailed comparison with [O III]λ5007 observations shows that the hot interstellar medium (ISM) is spatially anticorrelated with the [O III]-emitting clouds and has thermal pressures comparable to those of the [O III] media, suggesting that the hot ISM acts as a confining medium for the cooler photoionized clouds. The abundance ratios of the hot ISM are fully consistent with the theoretical values for enrichment from Type II supernovae, suggesting that the hot ISM is a wind from the starburst circumnuclear ring. X-ray emission from a ∼450 pc long nuclear radio jet is also detected to the southeast.

Key words: galaxies: active – galaxies: individual (NGC 1365) – galaxies: starburst – X-rays: galaxies – X-rays: ISM

Online-only material: color figures

1. INTRODUCTION

Understanding active galactic nucleus (AGN)–galaxy interaction and feedback is of great consequence for the study of both galaxy and AGN evolution (e.g., Silk & Rees 1998; Kauffmann et al. 2003; Hopkins et al. 2006). The intense ionizing radiation, relativistic jets, and winds from the AGNs interact with the interstellar medium (ISM) of their host galaxies, and may either stimulate or suppress star formation (e.g., Sazonov et al. 2004). Visible signatures of direct AGN–host interaction include kpc-scale regions with [O III] and Hα line emission, known as the extended narrow line region (ENLR), which have been found in many nearby Seyfert galaxies (Schmitt et al. 2003; Veilleux et al. 2003). Soft X-ray emission is seen associated with the ENLR, providing an opportunity to obtain X-ray diagnostic of the physical properties of the interacting ISM (e.g., Young et al. 2001; Yang et al. 2001; Ogle et al. 2000, 2003; Bianchi et al. 2006; Evans et al. 2006; Kraemer et al. 2008). Another important link between AGNs and starbursts is that molecular gas accreted to the nuclear region may induce a starburst (Elmegreen 1994), feed a central AGN, or both. AGN-related shocks may further stimulate star formation (e.g., Scoville 1992; González Delgado et al. 1998; Veilleux et al. 1995; Veilleux 2001). Star formation in the disks and galactic winds in hot halos of spiral galaxies can be traced by the diffuse X-ray emission as well (e.g., Tyler et al. 2004, Strickland et al. 2004; Swartz et al. 2006; Warwick et al. 2007). NGC 1365, the object studied in this paper, is ideal for these investigations, since it hosts an AGN and also has IR emission coincident with active, intensive nuclear star formation.

NGC 1365 is a nearby ($D = 18.6 \pm 1.9$ Mpc, $1'' \sim 90$ pc; Madore et al. 1998, 1999; Silbermann et al. 1999) archetype barred spiral galaxy (SBb(s)I; Sandage & Tammann 1981), and likely a member of the Fornax cluster (Jones & Jones 1980). A thorough review of the NGC 1365 galaxy is given in Lindblad (1999). It hosts vigorous star formation in the circumnuclear region and a variably obscured Seyfert 1.5 nucleus[4] (Veron et al. 1980; Hjelm & Lindblad 1996; Risaliti et al. 2007). The spectacular symmetric main spiral arms extending from the ends of a strong bar are apparent in the *XMM-Newton* Optical Monitor (OM) images (Figure 1). Dark dust lanes run across the nuclear region and partially obscure the nucleus.

NGC 1365 has long been known to exhibit a biconical outflow (Burbidge & Burbidge 1960; Phillips et al. 1983; Storchi-Bergmann & Bonatto 1991). A ∼5″ long (∼450 pc) 100° wide conical [O III]λ5007 emission-line region (ELR) is present to the southeast (SE) and to the northwest (NW) of the nucleus (Hjelm & Lindblad 1996; Kristen et al. 1997; Schulz et al. 1999; Veilleux et al. 2003), which suggests an AGN ionization cone, although a starburst-driven outflow explanation has also been advanced (Komossa & Schulz 1998). In the *Hubble Space Telescope* (*HST*) images, the inner 3″ of the conical outflow seen in [O III] is resolved into a number of small clouds and larger agglomerations (Kristen et al. 1997). A high-excitation [N II]λ6583/Hα region is aligned with the [O III] structure, but appears to be rectangular (Veilleux et al. 2003). Sandqvist et al. (1995) show that the inner parts of the [O III] region contain a

[4] Other classifications exist in the literature. For example, Turner et al. (1993) and Maiolino & Rieke (1995) classified the NGC 1365 nucleus as a Seyfert 2 and 1.8, respectively.

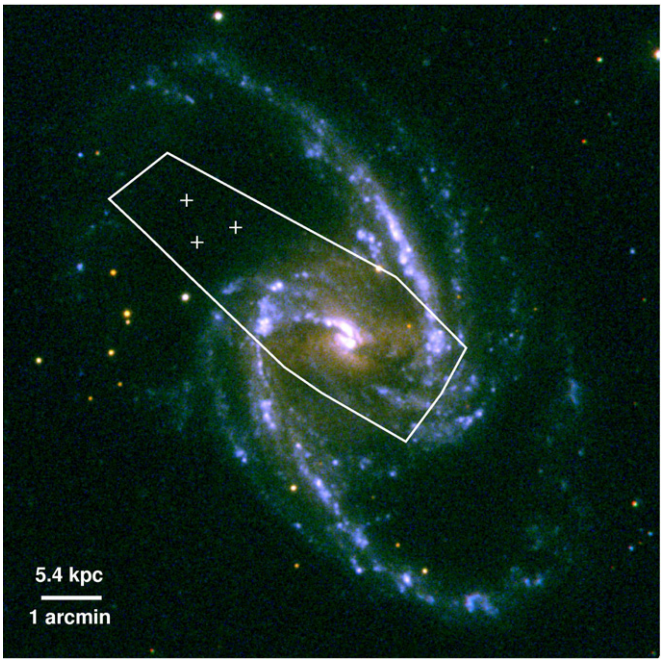

Figure 1. Composite ultraviolet (*UV*) image of NGC 1365 from *XMM Newton*/OM. Red corresponds to the *U* filter, green to the *UVW*1 filter and blue to the *UVM*2 filter. The area covered by all seven Chandra fields is outlined by a white polygon. The centers of background extraction regions are marked with plus symbols (see text). The image is $\sim 10' \times 10'$. North is up and east to the left.

(A color version of this figure is available in the online journal.)

nuclear radio jet, extending 5″ SE along the galaxy minor axis. Note that the spatial properties of the NGC 1365 galaxy and the outflow cones are well determined from these multiwavelength studies (see Lindblad 1999 review and references therein): the position angle (P.A.) of the line of nodes is ≈220°, and the inclination angle of the galaxy is 40°; the [O III] cone extends from the nucleus out of the galactic plane with its symmetry axis closely aligned with the rotation axis of the galaxy, with a full opening angle of about 100°; the counter cone to the NW is partially obscured by the absorbing dust in the galaxy plane.

Another prominent characteristic of NGC 1365 is the circumnuclear star-forming ring with a diameter of ∼ 14″ (∼ 1.3 kpc; Kristen et al. 1997). The kpc-size nuclear vicinity contains bright optical "hot spots" (Sérsic & Pastoriza 1965; clearly visible in the UV images shown in Figure 1). The circumnuclear regions are resolved into many compact super star clusters (Kristen et al. 1997), forming an elongated ring surrounding the AGN. Its minor axis is parallel to both the bicone axis and the galaxy minor axis, suggesting the possibility of a collimating torus (Sandqvist 1999). High resolution mid-infrared imaging of the ring (Galliano et al. 2005, 2008) also unveils a circumnuclear population of pointlike sources coincident with bright CO spots (Sakamoto et al. 2007) and nonthermal radio continuum sources (Sandqvist et al. 1995; Forbes & Norris 1998), which are interpreted as embedded young massive star clusters. The biconical ELR/outflow and the circumnuclear ring should be readily detectable in the *Chandra* images as hinted from the spatially extended X-ray emission in the *ROSAT* HRI image (Stevens et al. 1999).

In this paper, we present a high spatial resolution X-ray imaging study of the complex circumnuclear region of the active galaxy NGC 1365 with the *Chandra X-ray Observatory*. NGC 1365 has received a great deal of attention as a result of X-ray observing campaigns to monitor the obscuration of the AGN (e.g., Risaliti et al. 2005a, 2005b; Risaliti et al. 2007). Comparing to observations of NGC 1365 from previous generation X-ray satellites and the *XMM-Newton* observatory, the *Chandra* images offer an unprecedented view of the innermost regions of NGC 1365, which is critical to disentangle the different emission components.

Table 1
Log of *Chandra* ACIS-S Observations of NGC 1365

Obs ID[a]	Date	Pointing R.A.	Decl.	Roll Angle (°)	Good Time Interval (ks)
3554	2002 Dec. 24	53.409638	−36.147430	321.9	13.0
6868	2006 Apr. 17	53.399219	−36.139588	215.0	14.6
6869	2006 Apr. 20	53.399299	−36.139509	211.8	15.5
6870	2006 Apr. 23	53.399377	−36.139370	208.1	14.6
6871	2006 Apr. 10	53.399118	−36.139908	223.9	13.4
6872	2006 Apr. 12	53.399126	−36.139825	221.3	14.6
6873	2006 Apr. 15	53.399201	−36.139764	218.4	14.6

Notes. [a]ObsID 3554 is done with full ACIS-S array, while the rest observations were done in 1/4 subarray mode. All observations are performed in "Timed Event, Faint" mode.

2. OBSERVATIONS AND DATA REDUCTION

NGC 1365 was first imaged in 2002 with the back-illuminated chip of the Advanced CCD Imaging Spectrometer spectroscopy array (ACIS-S; Garmire et al. 2003) positioned at the focal point of *Chandra X-ray Observatory* high resolution mirror assembly (van Speybroeck et al. 1997; Weisskopf et al. 2002). It was further monitored with six *Chandra*/ACIS-S observations in "1/4 window" mode during 2006 April, resulting in a total exposure time of ∼100 ks (see Table 1 for details; the overlap region common to these observations is outlined in Figure 1).

The data products were analyzed with the *Chandra* X-Ray Center (CXC) CIAO v4.0 software and HEASOFT v6.4 package.[5] The new release of calibration files CALDB[6] v3.4.3 were used. The data were processed by the CXC (ASCDS version 7.6.7–7.6.9); verification and validation of the data products showed no anomalies. Following the standard *Chandra* ACIS data preparation thread, we reprocessed all level 1 data to create new level 2 events for consistency. A preliminary run of CIAO tool *wavdetect* (Freeman et al. 2002) is done for point source detection in the central 8′ region of each observation. A 10′ radius circle centered at the S3 aim point was used to query the Naval Observatory Merged Astrometric Dataset (NOMAD) catalogue (Zacharias et al. 2004), and the extracted optical sources are searched for counterparts to *Chandra* detections. Using optical point sources in the field detected in X-rays, the absolute astrometry for Observation ID (ObsID) 3554 is measured to be accurate to within 0.″5. By comparing the positions of the bright pointlike X-ray sources in common between observations, we then corrected the absolute astrometry for any relative offsets between the 2006 data sets and ObsID 3554. The relative shifts were ∼1 pixel.

To remove periods of high background, for each ObsID we extracted a light curve for chip S3, excluding any bright sources in the field. The light curves for 2006 observations showed no strong flares. However, a period of enhanced background was

[5] See http://cxc.harvard.edu/ciao/ and http://heasarc.gsfc.nasa.gov/lheasoft/ for more information.
[6] http://cxc.harvard.edu/caldb/

present in the last quarter of ObsID 3554, and 1.6 ks exposure of affected data was screened out. Finally all seven observations were merged into a single event file after correcting the relative astrometric offsets. Detailed study of the point source population is deferred to a future paper (J. Wang et al. 2009, in preparation; see also Strateva & Komossa 2009), which will also use the *XMM-Newton* observations of NGC 1365.

In addition to *Chandra* data, ancillary UV and mid-IR images were also used in this paper. NGC 1365 was observed with the *Spitzer Space Telescope* (SST, Werner et al. 2004) as part of a survey of luminous infrared galaxies (LIRGs; $L_{\rm IR} \geqslant 10^{11}\ L_{\odot}$)[7]. Observations with the Infrared Array Camera (IRAC; Fazio et al. 2004) were dithered to correct for cosmic ray events and bad pixels, and raster mapping was used to construct mosaics of the galaxy at 3.6, 4.5, 5.8, and 8.0 μm (Spitzer Astronomical Observation Request No. 12346880). Details of the IRAC observations and data processing are described by Mazzarella et al. (2008, in preparation). The *XMM-Newton* OM data were acquired from *XMM-Newton* ObsID No. 0205590301 (PI: G. Fabbiano), using the Processing Pipeline System (PPS) products processed with Science Analysis System (SAS; version 6.5.0). The UV images shown in Figure 1 used the following OM filters (Mason et al. 2001): *U* ($\lambda_0 \sim 3472$ Å), *UVW1* ($\lambda_0 \sim 2950$ Å), and *UVM2* ($\lambda_0 \sim 2298$ Å).

3. THE X-RAY COLOR IMAGES AND MORPHOLOGY

Smoothed images of the NGC 1365 region were first created without removing the point sources. This enabled us to examine the spatial distribution of the point sources with respect to the galaxy. We extracted images from the merged data in the commonly used soft band (0.3–0.65 keV), the medium band (0.65–1.5 keV), and the hard band (1.5–7 keV). Note that the medium band encompasses the emission from the Fe-L blend. The 0.3 keV low-energy boundary is the lowest energy where ACIS remains well calibrated, and the high energy 7 keV cutoff is chosen to limit the contribution from the background.

To derive exposure-corrected images, exposure maps were created for individual observations and bands, then reprojected to create the combined exposure maps matching the merged data. The band-limited images were then divided by the appropriate exposure maps and adaptively smoothed. This process enhances faint extended features while preserving the high resolution of brighter features. In order to prevent large variations in the adaptive smoothing scales between the bands with different counts, we applied to the soft and hard bands the same smoothing scales calculated for the medium-band image, which has the best signal-to-noise ratio (S/N). The significance was chosen between 2.4σ and 5σ above the local background (corresponding to the smoothing Gaussian kernel of varying scales between 1 and 40 pixels). Figure 2 presents the "false color" composite image of the central $3' \times 3'$ region of NGC 1365, where the soft-, medium-, and hard-band-smoothed images are shown in red, green, and blue, respectively. Besides the bright nucleus (marked as "N" in Figure 2), some 40 point sources are present. The bright off-nuclear X-ray source toward the lower right corner is a well-studied, variable ultraluminous X-ray source (ULX) NGC 1365 X-1 (Komossa & Schulz 1998), most likely a 50–150 $M_{\odot}$ accreting black hole (Soria et al. 2007).

Figure 2 shows the circumnuclear ring (mainly pink; $\sim 14''$ in diameter), intersected by the obscuring dust lane (blue). This ring is emphasized with an alternative set of energy bands shifted

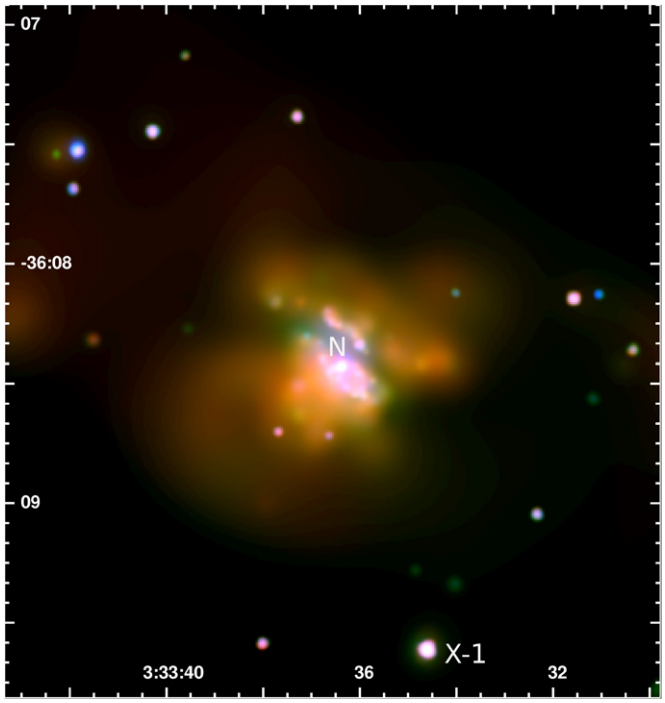

Figure 2. Adaptively smoothed image showing point sources and diffuse emission in the inner $3' \times 3'$ region of NGC 1365. Red represents soft-band X-ray emission (0.3–0.65 keV), green represents medium-band X-ray emission (0.65–1.5 keV), and blue for hard-band emission (1.5–7.0 keV).

(A color version of this figure is available in the online journal.)

to higher energies images in Figure 3, in which the soft band (red) is 0.3–1.5 keV, the medium band (green) is 1.5–3.0 keV, and the hard band (blue) is 3.0–7.0 keV; the same smoothing was applied as for Figure 2. The hard emission (presumably from young supernovae remnants and X-ray binaries) is less affected by the obscuration from the dust lane, tracing the extent of the star-forming ring. Note that with this energy band selection the (broader) soft band now has the best S/N of the three bands and so the smoothing scales from this band were used to smooth the images in the other two bands. This alternate band selection is only used here in this paper.

Comparison with *Spitzer* data clearly relates the hard X-ray ring to the circumnuclear star-forming ring prominent in the IR. Figure 4 shows the *Chandra* X-ray image of the diffuse emission (from Figure 6) in NGC 1365 (green/blue), together with the mid-IR (8 μm) view of the galaxy (red). Figure 5 zooms in to the central 1 arcmin, which shows a composite mid-IR image of the circumnuclear ring and a composite mid-IR/UV image of the same region with an overlay of the medium-band X-ray emission.

The circumnuclear ring is compact and maintains regularity close to the center. Such circumnuclear star formation rings are commonly observed in strongly barred spirals and assumed to be dynamically associated with the inner Lindblad resonance (ILR)–inflowing gas accumulates to form a massive star-forming ring between the two inner resonances (see Lindblad 1999). The inner ILR and outer ILR in NGC 1365 are $\sim 3''$ and $\sim 30''$ from the nucleus, respectively (Lindblad et al. 1996), hence the ring is located $\sim 4''$ outside of the inner ILR. We note a hot spot located at $\sim 22''$ (~ 2 kpc) northeast of the nucleus, which shows cospatial X-ray, UV, and mid-IR emission. IR filaments bridge the ring and this object, suggesting that it is related to the galaxy, instead of being a background object, and may be

[7] http://goals.ipac.caltech.edu/spitzer/Spitzer.html

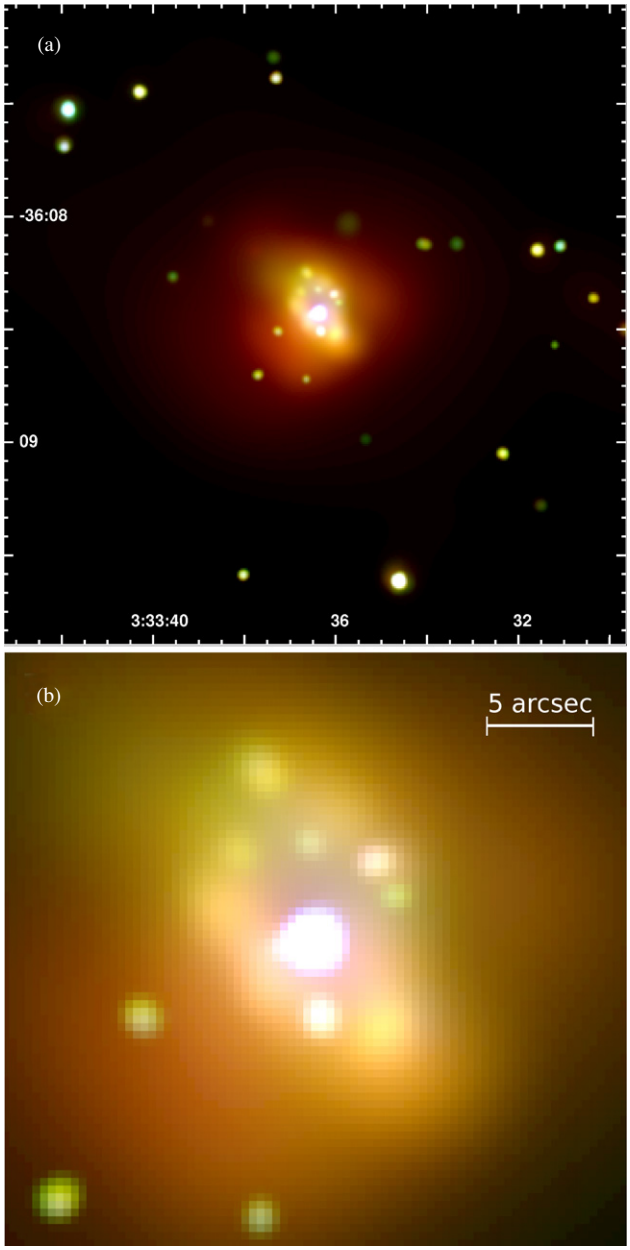

Figure 3. (a) Adaptively smoothed image of the same region in Figure 2, but with a different energy–color mapping. Here red refers to 0.3–1.5 keV emission, green is 1.5–3.0 keV, and blue 3.0–7.0 keV. (b) Same as (a) but zoomed-in to the inner $30'' \times 30''$ region showing the circumnuclear ring.

(A color version of this figure is available in the online journal.)

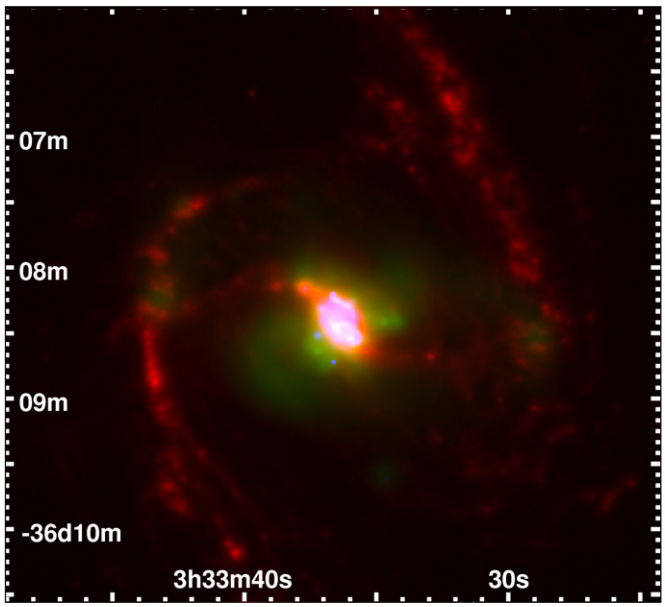

Figure 4. A $4' \times 4'$ *Spitzer* mid-IR and *Chandra* X-ray composite image of NGC 1365. Red is 8 μm mid-IR emission, green is medium-band X-ray emission, and blue is hard-band X-ray emission.

(A color version of this figure is available in the online journal.)

associated with the bar. The spatial correlation between the X-ray and UV emission is apparent. Because of the obscuring dust lane, which is traced by its bright IR emission, a bright ridge of X-ray/UV emission with hot spots appears coincide with the edge of the IR ring $\sim 10''$ (1 kpc) north and NW of the nucleus, probably related to the discrete regions of active star formation associated with the ring.

To study the large-scale diffuse emission, we followed the procedure of Baldi et al. (2006a) to create mapped-color images with point sources removed. Given the short individual exposure times, we performed point source detection in the combined exposures in the full band (0.3–7.0 keV). The pointlike ACIS detections including the nucleus were then removed from the data, and the resulting holes were filled by interpolating the surrounding background emission. The same procedure to define source regions and background regions employed by Baldi et al. (2006a) was followed. The results were visually compared with the band-limited images and the smoothed images to ensure that no apparent individual point sources were missed. In the circumnuclear ring region, a few "point" sources detected by *wavdetect* appear extended. These could be either association of unresolved point sources or bright patches and knots of diffuse emission. To check whether they affect the spectral analysis of the circumnuclear ring, we created separate event files without removing these sources with uncertain classification. These event files were used in spectral extraction and fitting described later in this paper.

The images with point sources removed and holes filled in the three bands (0.3–0.65 keV; 0.65–1.5 keV; and 1.5–7 keV) were adaptively smoothed, then combined to create a "mapped-color" image of the diffuse emission shown in Figure 6. The mapped-color image shows complex morphology and striking substructures that have not been seen in lower resolution X-ray images previously.

The overall morphology of the X-ray emission is rather consistent with the optical picture described in Section 1.

1. Extended soft X-ray emission appears to resemble a bicone (NW and SE) structure with the apex at the nucleus. The SE structure is more extended ($\sim 0\farcm8$ measured from the nucleus) and visually closer to a cone shape. Its inner region is brighter and appears to contain a substructure. The NW cone is only bright at the base close to the nuclear region ($\sim 0\farcm4$), with fainter emission extends toward far NW. Both cones are incomplete, possibly due to obscuring material in the galaxy plane and bulge. The measured projected half opening angle of the cone in the X-ray image is approximately $\sim 55^\circ$. The X-ray cones appear to be edge-brightened, which is consistent with the hollow cones seen in the optical (Lindblad 1999).
2. Harder X-ray emission is associated with the circumnuclear star-forming ring, which appears pink and clumpy in the image.

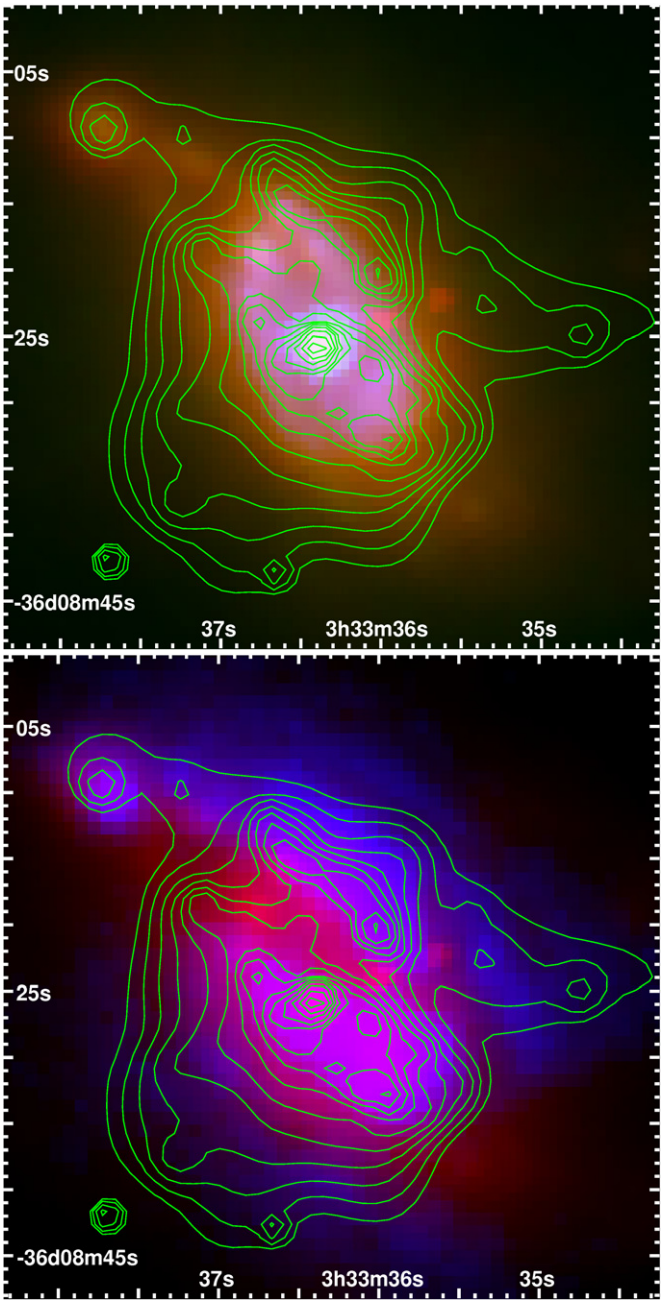

Figure 5. Top: *Spitzer*/IRAC composite image of the central 1 arcmin region of NGC 1365. Red is 8 μm emission, green is 4.5 μm, and blue 3.6 μm. Bottom: Composite mid-IR/UV image of the same region. Red is *Spitzer*/IRAC 8 μm image, and blue is *XMM*-Newton/OM *U*-band image. The X-ray contours (medium-band, without removing point sources) are shown in both panels to facilitate comparison.

(A color version of this figure is available in the online journal.)

3. The hardest X-ray emission, which appears as a $\sim$4″ wide blue band intersecting the top portion of the circumnuclear ring, is coincident with the dust extinction lane of the galaxy.

4. THE LINE-STRENGTH MAP

A quick examination of the spectra extracted from the diffuse emission shows the presence of the oxygen+iron+neon (O+Fe+Ne) emission blend (0.6–1.16 keV), the magnesium (Mg)-XI (1.27–1.38 keV) and the silicon (Si)-XIII (1.75–1.95 keV) lines (Figure 9). To identify regions of strong apparent line emission and to select possible anomalous abundance regions for spectral analysis, we generated an emission-line map, following Fabbiano et al. (2004) and Baldi et al. (2006a), to highlight regions of prominent emission lines in the hot ISM.

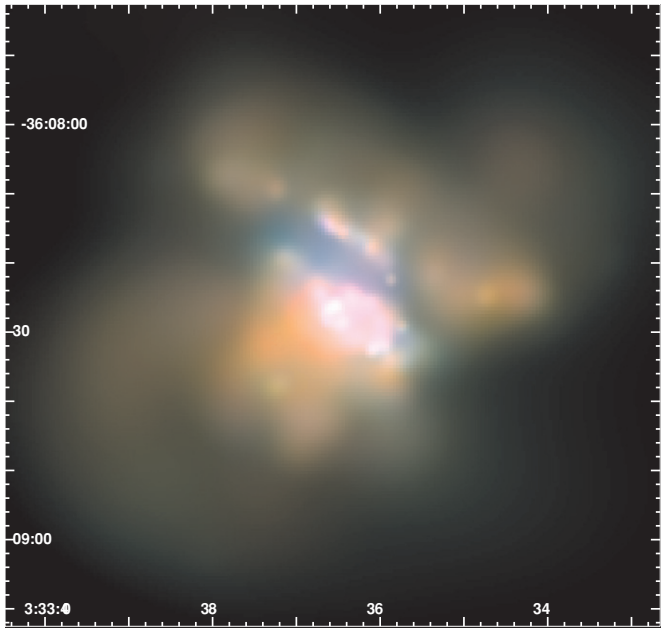

Figure 6. Adaptively smoothed image of the diffuse emission in NGC 1365. Point source have been removed. Two conical structures (with $\sim$ 100° opening angles) are seen extending toward NW (top right) and SE (lower-left) from the center. Red represents soft-band X-ray emission (0.3–0.65 keV), green medium-band X-ray emission (0.65–1.5 keV), and blue hard-band emission (1.5–7.0 keV).

(A color version of this figure is available in the online journal.)

Three band-limited images were created to encompass the lines noted above. A "continuum template" was extracted using the 1.4–1.65 keV and 2.05–3.05 keV bands which are not visibly contaminated by emission lines, and was used to determine the underlying continuum in the emission-line bands. All pointlike sources were removed and the holes were filled with a background as described in Section 3. The O+Fe+Ne 0.6–1.16 keV band image contains the largest number of counts and so was used to set the smoothing scales for the other line and continuum images.

To determine the continuum contribution in each line image, we extracted the spectrum of the entire diffuse emission of NGC 1365 and fitted the continuum with a simple two-component thermal bremsstrahlung model, excluding the three energy ranges with strong line emission. The best-fit model provides the appropriate scaling factors between the continuum level in our continuum template and the continuum in a given line band. The scaling factors are 2.5, 0.2, and 0.19 for the 0.6–1.16 keV, 1.27–1.38 keV, and 1.75–1.95 keV band, respectively. Each line image was continuum subtracted after weighting the continuum image by these scaling factors, and the resulting images were combined to create a mapped-color line-strength image (Figure 7).

Figure 7 shows that the emission-line structure of the hot ISM in NGC 1365 is also quite complex. Silicon emission (blue) appears most pervasive in the dust lane; this could be due to obscuration of the softer energy photons in this region, and this possibility is explored further below. Magnesium lines (green) and O+Fe+Ne emission (red) are prevalent in most regions. Part

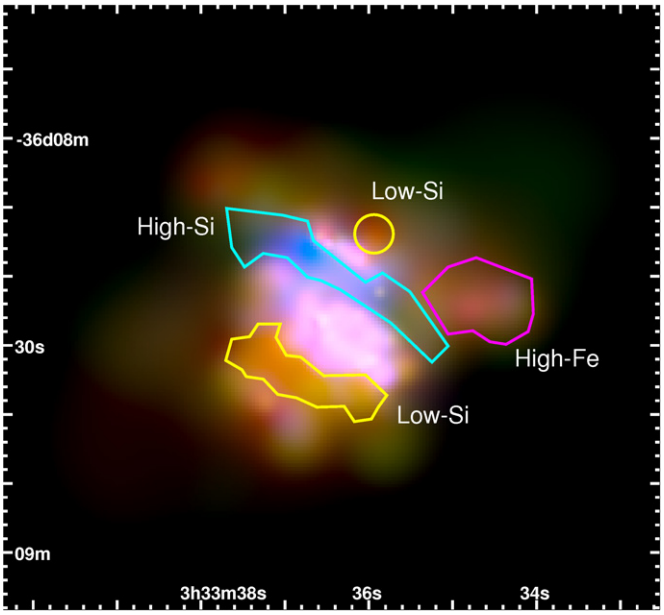

Figure 7. Adaptively smoothed image of the X-ray emission-line images in NGC 1365. Red represents Oxygen+Iron+Neon (O+Fe+Ne) emission blend (0.6–1.16 keV), green represents Magnesium (Mg)-XI (1.27–1.38 keV) line, and blue represents Silicon (Si)-XIII (1.75–1.95 keV). The overlaid polygons outline the extreme line ratio regions for further spectral analysis.

(A color version of this figure is available in the online journal.)

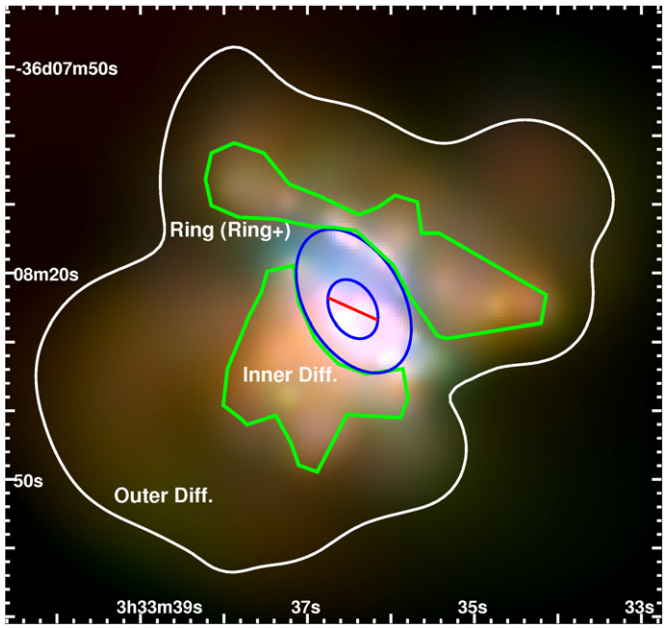

Figure 8. Diffuse emission image overlaid with the regions used for spectral extraction. The "ring" is outlined by the blue ellipse excluding the central nucleus. The region "diffuse" refers to all the diffuse emission, excluding the area inside the outer limit of the ring. It is further divided to "inner diffuse" (the bright portion of the cones; green polygons) and "outer diffuse" (the remaining faint diffuse emission).

(A color version of this figure is available in the online journal.)

of the NW diffuse region shows enhanced O+Fe+Ne emission. Noticeably, there is an area (orange in color) south of the star-forming ring that is lacking in silicon line emission.

5. SPECTRAL ANALYSIS

5.1. Data Extraction

The mapped-color X-ray image (Figure 6) and the line-strength map (Figure 7) demonstrate that the diffuse emission of the hot ISM in NGC 1365 is rich in spatial and spectral features. These figures suggest a structure in the hot ISM, possibly the effect of varying absorption columns, plasma temperatures, and metal enrichment.

As outlined in Figures 8 and 7, we identified five separate regions based on morphology and three regions based on apparent abundance pattern to perform spectral analysis of the X-ray emission from the hot ISM. The region "ring" refers to the circumnuclear ring, excluding the nucleus (see Section 3 and Figure 3). The region "diffuse" refers to all the diffuse emission, excluding the area inside the outer limit of the ring. It is further divided into "inner diffuse" (the bright portion of the cones) and "outer diffuse" (the faint diffuse emission). In addition, for the ring area we also extracted photons from the "ring" region including the *wavdetect* selected point sources that appear extended (see Section 3). We dubbed the region and the corresponding extraction "ring+." We did not further divide the diffuse emission into subregions (e.g., the ring is separated by the dust lane into north ring and south ring) to have good statistics for the spectral fitting. Regions related to the emission-line features noted in Figures 7 were also created, with descriptive names (high Si, low Si, and high Fe). We emphasize here that, even though the extended emission is referred to as "diffuse," the X-ray emission is not *bonafide* diffuse plasma. There is evidence for extensive clumpiness and X-ray hot spots. The "diffuse" X-rays include a mixture of hot ISM and unresolved point sources (XRB/SNR) associated with regions of very active star formation. The hard power-law component seen in the spectral fit (see Section 5.2) is likely related to the XRB/SNR components.

We extracted spectra separately from the individual ObsIDs for each diffuse emission regions described above. We excluded all the point source areas above 3σ described in Section 3. We also extracted background counts representative of the field from three circular source-free regions (each with a 0.′4 radius, resulting in a total area of 1.5 arcmin^2) well outside the galaxy, but within the ACIS-S3 chip in all seven observations (Figure 1). A new CIAO script *specextract*[8] was used to extract the region spectra for multiple observations. This script extracts the spectrum and creates area-weighted Response Matrix Files (RMF) and Ancillary Response Files (ARF) for each region. For each region of interest, all source spectra and background spectra were co-added, and the response files were combined with their appropriate weights using the FTOOLS software[9]. The resulting spectra were then grouped so as to have a signal-to-noise ratio S/N $\geqslant$ 10 in each energy bin.

5.2. Thermal and Power-Law Models

The extracted spectra were analyzed with XSPEC v12.0 (Arnaud 1996), using combinations of absorbed optically thin thermal emission and power-law components to fit the data. We used the Astrophysical Plasma Emission Code (APEC) thermal-emission model (Smith et al. 2001) that utilizes improved atomic data from the Astrophysical Plasma Emission Database.[10] The absorption column was modeled with *tbabs* (Wilms et al. 2000), which includes updated photoionization cross section

[8] See CIAO thread http://cxc.harvard.edu/ciao/threads/specextract/.
[9] http://heasarc.gsfc.nasa.gov/docs/software/ftools/
[10] http://cxc.harvard.edu/atomdb/

Table 2
Best-Fit Parameters (1.65σ errors for one interesting parameter) for the Diffuse Emission of NGC 1365

Region	Net Counts	χ^2/dof	$N_{\rm H}$ ($\times 10^{20}$ cm^{-2})	kT (keV)	Z_O ($\times Z_{\rm O,\odot}$)	$Z_{\rm Ne}$ ($\times Z_{\rm Ne,\odot}$)	$Z_{\rm Mg}$ ($\times Z_{\rm Mg,\odot}$)	$Z_{\rm Si}$ ($\times Z_{\rm Si,\odot}$)	$Z_{\rm Fe}$ ($\times Z_{\rm Fe,\odot}$)	Γ	Mod[a]
Diff.	8216 ± 224	44.7/50	$3.59^{+4.71}_{-2.60}$	$0.57^{+0.05}_{-0.03}$	$0.38^{+0.17}_{-0.21}$	$0.20^{+0.17}_{-0.15}$	$0.32^{+0.20}_{-0.17}$	$0.45^{+0.37}_{-0.32}$	0.18 ± 0.04	...	1T
Ring	5541 ± 184	21.8/31	$15.95^{+12.08}_{-9.65}$	0.61 ± 0.05	1.0	$7.73^{+3.59}_{-3.37}$	$6.65^{+4.27}_{-3.33}$	$14.74^{+7.72}_{-6.26}$	$3.06^{+2.31}_{-0.83}$	$2.65^{+0.72}_{-0.49}$	TP
Ring+	7524 ± 191	34.7/47	$11.29^{+6.63}_{-6.00}$	$0.61^{+0.03}_{-0.04}$	1.0	$3.39^{+8.71}_{-1.85}$	$3.17^{+5.99}_{-1.61}$	$6.23^{+10.6}_{-2.95}$	$1.41^{+0.53}_{-0.51}$	$2.35^{+0.48}_{-0.42}$	TP
Inner Diff.	5330 ± 242	22/32	$8.51^{+18.6}_{-3.83}$	$0.48^{+0.10}_{-0.17}$	$0.14^{+0.12}_{-0.07}$	$0.17^{+0.17}_{-0.15}$	$0.20^{+0.21}_{-0.15}$	$0.36^{+0.69}_{-0.31}$	0.10 ± 0.03	...	1T
Outer Diff.	3239 ± 198	19.8/25	1.34[a]	$0.57^{+0.05}_{-0.06}$	$0.58^{+0.37}_{-0.24}$	$0.24^{+0.34}_{-0.22}$	$0.49^{+0.37}_{-0.31}$	$1.02^{+0.99}_{-0.79}$	$0.22^{+0.07}_{-0.05}$	...	1T
High Si	1382 ± 165	18/38	$33.14^{+18.39}_{-23.77}$	$0.61^{+0.12}_{-0.10}$	1.0	1.0	$1.62^{+2.29}_{-0.86}$	$3.46^{+3.95}_{-1.82}$	$0.37^{+0.29}_{-0.16}$	...	1T
Low Si	1580 ± 166	19/39	1.34[a]	0.61 ± 0.06	1.0	1.0	$0.69^{+0.74}_{-0.65}$	0	$0.30^{+0.12}_{-0.09}$	...	1T
High Fe	498 ± 160	10/32	1.34[a]	0.46 ± 0.09	1.0	1.0	$0.67^{+3.77}_{-0.64}$	$1.91^{+51}_{-1.91}$	$0.32^{+0.97}_{-0.30}$	...	1T

Note. [a]Indicates freezed parameter. XSPEC Models: 1T = *tbabs(vapec)*; TP = *tbabs(vapec+powerlaw)*.

and abundances of the ISM, as well as a treatment of interstellar grains and the H_2 molecule.

We first considered absorbed single-temperature APEC models as well as two-temperature APEC models. A single line-of-sight absorption column was used in all cases, equivalent to Galactic line-of-sight column (1.4×10^{20} cm^{-2}; Kalberla et al. 2005) combined with the intrinsic absorption within NGC 1365, which was free to vary. When the fit required unmeasurably small absorption ($N_{\rm H} \ll 10^{20}$ cm^{-2}), we froze $N_{\rm H}$ at the Galactic column. As the spectrum of the integrated diffuse emission clearly shows prominent Mg XI (~1.3 keV), O VII–Ne IX/X-Fe-L complex (0.6–1.2 keV), and Si XIII (~1.8 keV) line features, the abundances of these elements were left to vary freely. When fitting with the two-component models, the oxygen abundance was fixed at the solar value as it is poorly constrained in our data and consistent with solar abundance. A power-law component is introduced to the single-temperature model to allow for the possible integrated emission of unresolved X-ray binaries that are too faint to be detected individually. A simple absorbed power-law model gives poor fits ($\chi^2_\nu > 4$) to all the extracted spectra. To fit the spectra of the three extreme line ratio regions (Figures 7), we only allow the abundances of Mg, Si, and Fe to vary, given the limited number of extracted counts.

For each of the regions used in the spectral analysis, the net counts (background subtracted) in the full band, the reduced χ^2 (χ^2 over the numbers of degrees of freedom (dof), χ^2_ν), the resulting best-fit temperature(s) kT (keV), absorbing column density $N_{\rm H}$ (cm^{-2}), and power-law photon index Γ (if a power-law component is invoked) are summarized in Table 2, together with the abundances of oxygen, neon, magnesium, silicon, and iron relative to the solar values. The last column of Table 2 gives the adopted "best-fit model," which is chosen based on having the smallest χ^2_ν. If more than one model can fit the spectrum well, and the χ^2_ν values are close (difference less than 0.1), a simpler model with less free parameters is preferred. The errors are quoted at 1.65σ (90% confidence interval) for one interesting parameter. The spectra of the regions, together with the best-fit models and the data−(best-fit-model) residuals, are shown in Figure 9.

In summary, these results show variations in different morphological/physical regions:

1. The large-scale diffuse emission (diffuse) is well fitted with a single-temperature thermal model, with a well determined $kT = 0.57^{+0.05}_{-0.03}$ keV. The absorption may be a little in excess of the Galactic column toward NGC 1365 ($\Delta N_{\rm H} = 2.2^{+4.7}_{-2.2} \times 10^{20}$ cm^{-2}). To adequately fit the emission lines in the ACIS spectrum, the data require subsolar abundances ($Z/Z_\odot \sim 0.2$–0.4). The subregions of the diffuse emission show similar characteristics to the combined emission. The absorption column of the outer diffuse emission ("outer diff") is low, consistent with just Galactic absorption, which is reasonable, as the region is further away from the spiral disk.
2. The spectra of the circumnuclear ring (and "ring+") require higher absorption columns, $\log N_{\rm H} \sim 21.2$ cm^{-2}, and a hard spectral component in addition to the $kT = 0.6 \pm 0.05$ keV thermal component similar to the diffuse emission ("diffuse"). The large $N_{\rm H}$ is not surprising given the dust lane and higher obscuration toward the nuclear region. In the power-law fit this hard component has a photon index $\Gamma \sim 2.5$; using a two-temperature thermal model, we obtain a hard $kT \sim 3$ keV, but the fit with power-law component has a better χ^2 for the same numbers of free parameters. In either case a hard component is required, and maybe due to the unresolved X-ray source population in the ring. The best-fit model suggests supersolar abundances in the hot ISM (~3 times $Z_\odot$).
3. For the extreme line ratio regions, all the fits have χ^2_ν less than 1 indicating the models are over complex for the data. Nevertheless, the "high-Si" region (dust lane) shows high-absorption column ($\log N_{\rm H} \sim 21.5$) as expected. The fit suggests under-abundant Fe, but this result may be affected by the obscuration of the dust lane. Taking the $N_{\rm H} = 3.2 \times 10^{21}$ cm^{-2} (Table 4) and a visual extinction $A_{\rm V} \sim 3$ mag (Roy & Walsh 1997; Kristen et al. 1997; Galactic contribution is removed from $N_{\rm H}$ and $A_{\rm V}$), we measured a gas-to-dust ratio $N_{\rm H}/A_{\rm V} \sim 10^{21}$ cm^{-2} mag^{-1}, which is roughly in agreement with the standard Galactic gas-to-dust ratio $N_{\rm H}/A_{\rm V} = 1.9 \times 10^{21}$ cm^{-2} mag^{-1} (Maiolino et al. 2001 and references therein). The extracted spectra of "low-Si" region also suggests extremely low abundance of Si ($Z_{\rm Si}/Z_\odot \sim 10^{-3}$ preferred from the fit; we consider it unconstrained). We note that a similar low-Si abundances have been reported in some regions of the Antennae (NGC 4038/9; Baldi et al 2006b). A possible explanation for this deficiency is that a large fraction of the silicon has cooled and locked in dust grains. SN Ia enrichment may also yield a relatively low-Si abundance (Nagataki & Sato 1998).
4. Lastly, for all the spectral fitting, we emphasize that the temperature and absorption column for the same region determined from various models show little variation, indicating that these parameters are rather robust.

In Table 3, we list the derived emission parameters from the spectral analysis of each region. From these emission parameters

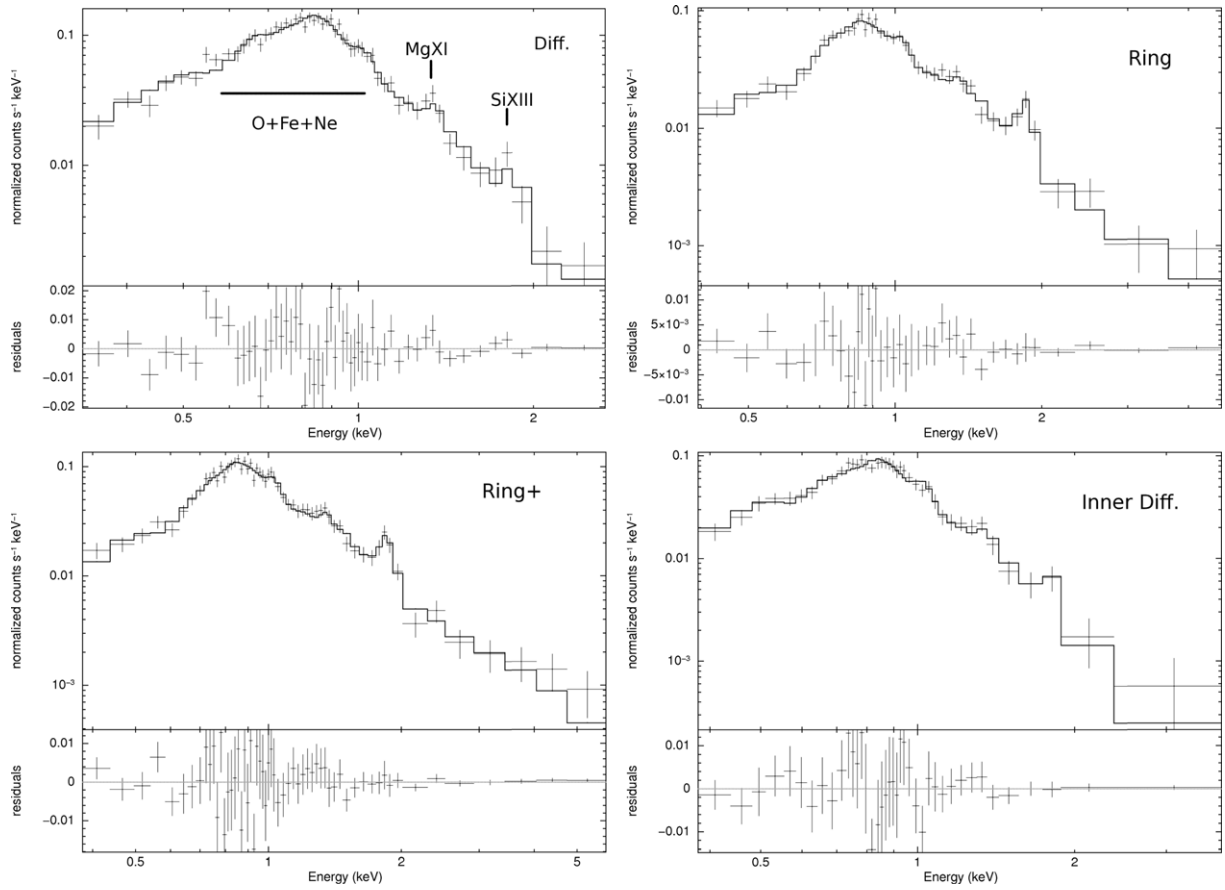

Figure 9. X-ray spectra and best-fits for the regions listed in Table 2.

Table 3
Emission Parameters for the Diffuse Emission in NGC 1365

Region	$F^{p.l.}_{0.3-10\ \mathrm{keV}}$ ($\times 10^{-14}$ erg cm^{-2} s^{-1})	$F^{\mathrm{therm}}_{0.3-10\ \mathrm{keV}}$ ($\times 10^{-14}$ erg cm^{-2} s^{-1})	$E.M.^{(*)}$ ($\times 10^{62}$ cm^{-3})	$L^{p.l.}_{0.3-10\ \mathrm{keV}}$ ($\times 10^{38}$ erg s^{-1})	$L^{\mathrm{therm}}_{0.3-10\ \mathrm{keV}}$ ($\times 10^{38}$ erg s^{-1})	$\frac{L^{p.l.}_{0.3-10\ \mathrm{keV}}}{L^{\mathrm{therm}}_{0.3-10\ \mathrm{keV}}}$
(1)	(2)	(3)	(4)	(5)	(6)	(7)
Diff.	...	$34.61^{+2.79}_{-5.40}$	$20.09^{+9.15}_{-4.25}$	...	$140.16^{+11.34}_{-21.87}$	...
Ring	$25.17^{+15.81}_{13.54}$	$11.59^{+7.32}_{-6.24}$	$0.93^{+0.26}_{-0.18}$	$101.96^{+64.00}_{-54.69}$	$46.95^{+29.57}_{-25.12}$	2.17
Ring+	$31.41^{+10.91}_{-14.70}$	$13.63^{+4.74}_{-6.39}$	$1.87^{+0.87}_{-0.71}$	$127.23^{+44.15}_{-59.54}$	$55.23^{+19.20}_{-25.88}$	2.30
Inner Diff.	...	$30.19^{+23.76}_{-30.19}$	$18.87^{+59.8}_{-8.54}$	...	$122.31^{+96.01}_{-122.31}$	...
Outer Diff.	...	$12.32^{+2.34}_{-3.95}$	$6.37^{+1.39}_{-1.20}$	...	$49.91^{+9.47}_{-16.00}$	...

Notes. Column 1: the name of the extracted region. Column 2: the observed 0.3–10 keV flux of the power-law component (if present). Column 3: the observed 0.3–10 keV flux of the thermal emission. Column 4: the emission measure defined as $E.M. = n^2V$. Column 5: the absorption-corrected luminosity (0.3–10 keV) of the power-law component. Column 6: the absorption-corrected luminosity of the thermal emission. Column 7: the ratio between the intrinsic luminosities (0.3–10 keV) of the power-law and the thermal emission.

and those listed in Table 2, following Fabbiano et al. (2003) and Baldi et al. (2006b), we can further estimate some physical properties of the emitting plasma, such as electron density n_e ($\approx n_H$), thermal energy content E_{th}, cooling time τ_c, pressure p, hot ISM mass M_{ISM}, and supernovae rate R_{SN}. These quantities are given in Table 4. The emitting volume (V) of the hot gas in the region of interest (assuming a cylindrical geometry) is derived using the projected area on the plane of the sky multiplied by a height of 200 pc (for the typical depth of a spiral disk). Considering the approximate nature of the geometry and depth of the hot gas, the inclination of the galaxy (~ 40 deg) has little effect on the estimated emitting volume. The filling factor η is assumed to be 100% in Table 4, and the derived parameters have weak dependence on η (n_e, $p \propto \eta^{-1/2}$ and E_{th}, τ_c, $R_{SN} \propto \eta^{1/2}$). These estimates assumed an η of unity and the geometry of the X-ray-emitting gas, and should not be treated as precise measurements (see discussion in Baldi et al. 2006b).

5.3. Photoionization Model

Although a thermal model accounts well for the bulk of the diffuse X-ray emission, some positive residuals are seen around 0.53 keV (N VII–O VII) and around 0.7–0.8 keV (possibly O VII and O VIII radiative recombination continua) in the thermal fit of diffuse emission (Figure 9), which hint at the presence of additional possible photoionized, emission lines. Emission from a photoionized medium might be the dominant component in the inner region around the nucleus (Guainazzi et al. 2009, in preparation), though not at radii greater than 10″. To explore

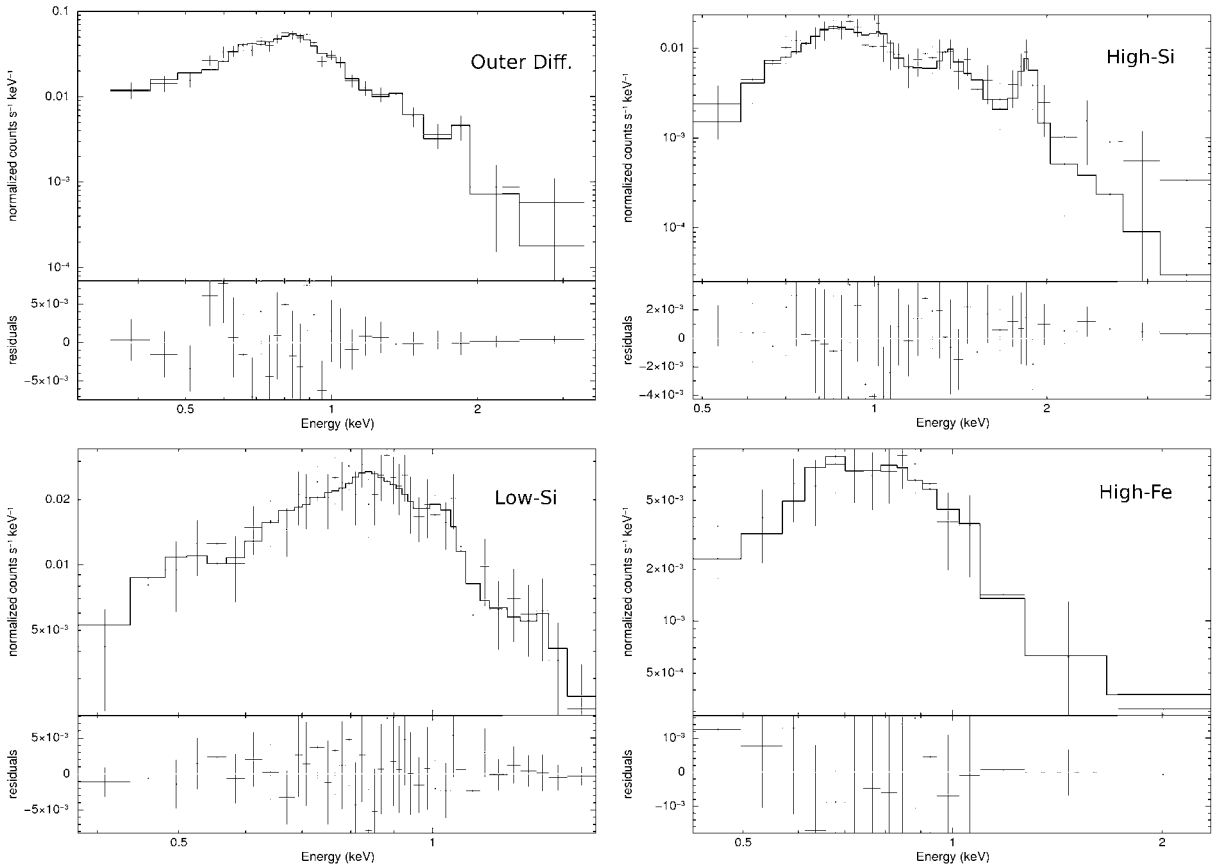

Figure 9. (Continued)

Table 4
Hot-Gas Parameters

Region	Area (kpc^2)	n_e ($\times 10^{-2}$ cm^{-3})	E_{th} ($\times 10^{54}$ erg)	τ_c ($\times 10^7$ yr)	p ($\times 10^{-10}$ dyne cm^{-2})	M_{ISM} ($\times 10^5$ $M_\odot$)	R_{SN} (10^{-3} yr^{-1})
(1)	(2)	(3)	(4)	(5)	(6)	(7)	(8)
Diff.	29.2	10.8	50.9	9.26	1.97	155.3	7.3
Ring	1.1	11.9	2.3	8.64	2.34	6.5	0.3
Ring+	1.3	15.6	3.5	6.62	3.06	10.0	0.5
Inner Diff.	5.8	23.5	18.9	3.95	3.69	67.1	2.7
Outer Diff.	23.4	6.8	25.6	14.7	1.24	78.3	3.7

Notes. Column 1: the name of the extracted region. Column 2: the area of the extracted region (assuming a distance of $d \sim 18.6$ Mpc). Column 3: thermal gas electron density derived from the emission measure ($EM = n^2V$). Column 4: thermal energy contained in the gas. Column 5: cooling time of the hot gas, estimated following Tucker (1975). Column 6: thermal pressure ($p = 2nkT$) of the hot gas. Column 7: estimated mass of the hot ISM. Column 8: the SN explosion rate needed to provide mechanical energy deposited to the ambient ISM (see Heckman et al. 1996; Fabbiano et al. 1997).

the line emission from photoionized gas, we used XSTAR[11] (Kallman & Bautista 2001) v2.1ln7 and the XSPEC12 local model *photemis*[12] to model the photoionized contribution to the extended X-ray emission (diffuse and inner diffuse). Using a photoionized model alone yielded poor fits ($\chi^2_\nu \gg 5$) of the spectra (see further discussed from an energetic viability perspective in Section 6.1). Unlike in detailed photoionization modeling studies of high resolution grating spectra (e.g., Ogle et al. 2000, 2003), we froze the parameters in our best-fit thermal model and added an emission component from a warm photoionized emitter. We assume that the gas is photoionized by an incident spectrum with a power-law index $\Gamma = 1.7$ (consistent with the average spectral index of the nucleus, Risaliti et al. 2007), and calculated the photoionized emission with XSTAR. We find that the best-fit ionization parameter is $\log \xi = 0.5 \pm 0.4$, where $\xi = L/(nR^2)$, L is the luminosity of the ionizing source, n is the ion density, and R is the distance to the source. We estimate an emission measure $(E.M.) = 2 \times 10^{61}$ cm^{-3} for the photoionized emitter, about 1% of the $E.M.$ of the thermal component. Since the X-ray-absorbing gas toward NGC 1365 nucleus shows significant variability, we also attempted modeling with an incident spectrum of $\Gamma = 2.3$ (the spectral slope derived from high S/N *XMM*-Newton spectra with the lowest absorption column, which represents the best measurements of the continuum parameters; G. Risaliti et al. 2008, in preparation). The resulting ionization parameter is poorly constrained, $\log \xi = 0.2 \pm 1.2$, and the photoionized emitter may contribute ~17% of the total $E.M.$

[11] http://heasarc.gsfc.nasa.gov/docs/software/xstar/xstar.html
[12] Available at ftp://legacy.gsfc.nasa.gov/software/plasma_codes/xstar/warmabs21ln7.tar.gz

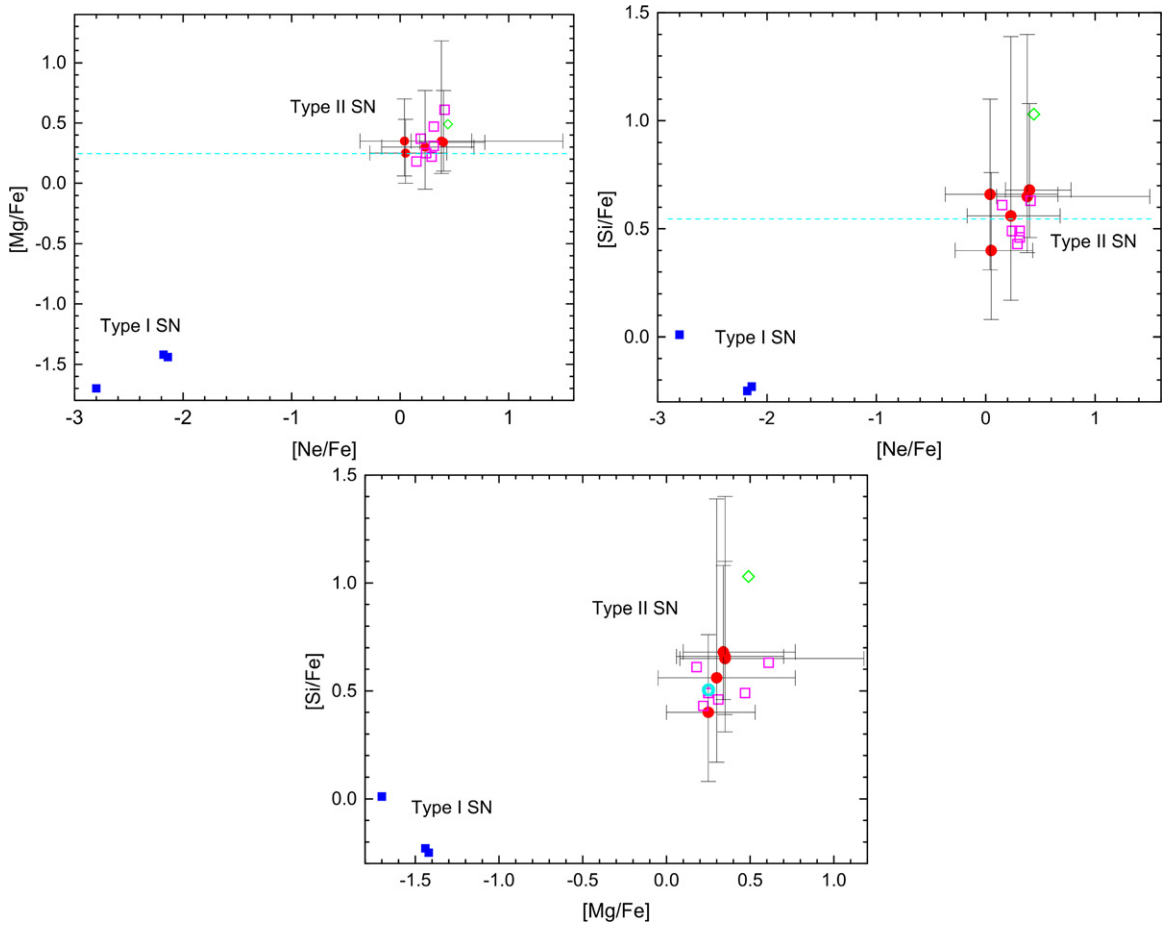

Figure 10. Abundace ratio diagrams for regions in NGC 1365: [Ne/Fe] vs. [Mg/Fe], [Ne/Fe] vs. [Si/Fe], and [Mg/Fe] vs. [Si/Fe]. Abundance units refer to meteoritic abundances of Anders & Grevesse (1989). The regions in Table 4 are plotted with filled circles (red). The ratios for stellar yields from SNe Type I (blue filled squares) and Type II (magenta open squares) are also shown, adopted from various theoretical works (see Table 5 for the list of references). Diamond (green; upper limit for [Si/Fe]) and open circle (cyan; line is used where no [Ne/Fe] measurement is available) denotes abundance ratio for Strickland et al. (2004) sample of starbursts and the warm Galactic halo, respectively.

(A color version of this figure is available in the online journal.)

6. DISCUSSION

6.1. The Nuclear Cone: Hot or Photoionized ISM?

A biconical ENLR is a common feature of nearby Seyfert galaxies (Schmitt et al. 2003), and the associated soft X-ray emission has been suggested to originate from the same photoionized gas seen in [O III] (e.g., Ogle et al. 2000; Bianchi et al. 2006). For the ionization cones in NGC 1365 (in the "diffuse" region), the soft emission is consistent with a thermal origin, as the thermal model provides an adequate fit to the spectra, while the pure photoionization model fails. Further morphological evidence from X-ray and [O III] emission will be discussed in the following section. The presence of the Fe-L complex, which is often seen dominant in spectra from hot gas in collisional ionization equilibrium (Phillips et al. 1982) supports a thermal origin, although Ogle et al. (2003) cautioned that these lines could arise from recombination and photoexcitation as well. *Chandra* observations of NGC 1068 (Ogle et al. 2003) demonstrated that AGN outflows can show a wide range in ionization ($\log \xi$ =1–3). The derived $\log \xi = 0.5 \pm 0.4$ (or $\log \xi = 0.2 \pm 1.2$ if $\Gamma = 2.3$) in our simple photoionization fitting (Section 5.3) is low but marginally consistent with the lower boundary of ξ.

Following Weaver et al. (1995) and Evans et al. (2006), we further examine the energetic viability of the photoionization model with the measured X-ray luminosity, assuming that the extended soft X-ray-emitting gas is predominantly photoionized by the nuclear emission. In this case, an ionizing parameter $\xi = 100$ ergs cm s^{-1} is required to produce the strong Fe-L emission feature arising from ionized gas (Kallman & McCray 1982). Adopting an emissivity $j(\xi) = 10^{-24}$ ergs cm^3 s^{-1} for the photoionized gas and the observed soft X-ray emission $L_X \sim 10^{40}$ ergs s^{-1}, we derived a density $n \sim 0.2$ cm^{-3}. It is worth noting that this density is in excellent agreement with the $n_e \sim 0.1$–0.2 cm^{-3} that we derived in the hot gas from the thermal model (Table 4), indicating that our estimate is reasonable despite the simple assumption made here. Substituting ξ, n, and a distance $R = 10''$ (900 pc) in $\xi = L/(nR^2)$, the luminosity of the nucleus required to photoionize the gas to the observed level is $L \sim 2 \times 10^{44}$ ergs s^{-1}. This is $\sim$100–1000 times higher than the unabsorbed $L_X \sim 10^{41}$–10^{42} ergs s^{-1} (2–10 keV) reported in Risaliti et al. (2005b), suggesting that photoionization alone cannot account for the extended soft X-ray emission unless the ionizing radiation from the nuclear source is highly anisotropic. As NGC 1365 is a relatively low-luminosity AGN, that thermal emission is dominant over an AGN-continuum photoionized gas may not be surprising. We note that NGC 1365 is characterized with a surface density of the star formation rate $\Sigma_{SFR} = 3\ M_\odot$ yr^{-1} kpc^{-2} and a mean gas surface density $\Sigma_{H_2} = 1 \times 10^3\ M_\odot$ pc^{-2} (Sakamoto et al. 2007; a

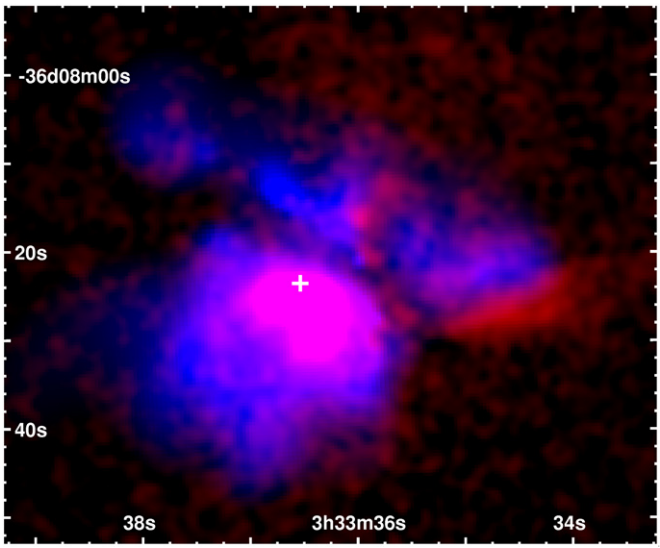

Figure 11. Composite image of the soft band (0.3–0.65 keV) X-ray emission (blue) and continuum-subtracted [O III] image (red). The plus symbol marks the position of the nucleus. Note how the X-ray morphology appears to complement the [O III] emission in the NW region. The [O III] image is from Veilleux et al. (2003).

(A color version of this figure is available in the online journal.)

^{12}CO-to-H_2 conversion factor is adopted as in Kennicutt 1998). These surface densities follow the Kennicutt–Schmidt law for a sample of starbursts and normal disk galaxies (Kennicutt 1998). Wang et al. (2007) derive a domain in the Σ_{SFR}–Σ_{H_2} plot where the circumnuclear medium is significantly affected by the AGN radiation, and with a sample of 57 Seyfert galaxies they show evidence that the circumnuclear star formation of many Seyferts is suppressed by the AGN feedback. We find NGC 1365 lies near but outside of the boundary of the AGN feedback domain, resembling the starbursts well.

Our spectral results are overall consistent with previous X-ray studies of NGC 1365 that found that the extended soft nuclear emission can be well fitted by a thermal plasma model with a very low local absorbing column (Fabbiano et al. 1992; Iyomoto et al. 1997; Komossa & Schulz 1998; Stevens et al. 1999). We caution that the low resolution CCD imaging spectroscopy cannot distinguish whether the "continuum" is actually made of unresolved emission lines from photoionized gas. Higher resolution grating spectra, especially constraints from the line intensities can shed more light on the AGN-photoionized emission component (e.g., Guainazzi & Bianchi 2007; Evans et al. 2007; Longinotti et al. 2007; Kraemer et al. 2008).

Additional evidence in favor of a thermal hot ISM can be gathered by comparing our results with the [O III] properties of the circumnuclear region. Figure 11 compares the spatial correspondence between the X-ray emission and continuum-subtracted [O III] image from Veilleux et al. (2003), enabled by the superior arcsec resolution X-ray image and the excellent astrometry. Both X-ray and [O III] are present in the inner 10″ region around the nucleus. Most importantly, the NW cone shows some complementary structure between the two types of emission (a 'Swiss-cheese"-like morphology): the X-ray emission is weak where the [O III] emission is strong. The hot X-ray-emitting gas appears delimited by the cooler condensation traced by the [O III] emission. This spatial anticorrelation cannot be attributed to obscuration or projection, and is consistent with a predominantly thermal origin for the X-ray emission (Elvis et al. 1983, Ogle et al. 2000), which was also suggested by our spectral analysis (Section 5).

Table 5
Comparison of Relative Element Abundances

Region (1)	[Ne/Fe] (2)	[Mg/Fe] (3)	[Si/Fe] (4)
All Diff.	$0.05^{+0.38}_{-0.33}$	$0.25^{+0.28}_{-0.25}$	$0.40^{+0.36}_{-0.32}$
All Ring	$0.4^{+0.38}_{-0.22}$	$0.34^{+0.43}_{-0.24}$	$0.68^{+0.40}_{-0.22}$
All Ring+	$0.38^{+1.12}_{-0.28}$	$0.35^{+0.83}_{-0.27}$	$0.65^{+0.75}_{-0.26}$
Inner Diff.	$0.23^{+0.45}_{-0.40}$	$0.3^{+0.47}_{-0.35}$	$0.56^{+0.83}_{-0.39}$
Outer Diff.	$0.04^{+0.62}_{-0.41}$	$0.35^{+0.35}_{-0.29}$	$0.66^{+0.44}_{-0.35}$
Hot halo emission S04[a]	0.44	0.49	< 1.03
Warm Galactic halo[b]	...	0.25	0.5
Type II SN A96[c]	0.19	0.37	...
Type II SN T95[c]	0.31	0.47	0.49
Type II SN W95A (10^{-4} $Z_\odot$)[c]	0.15	0.18	0.61
Type II SN W95B (10^{-4} $Z_\odot$)[c]	0.29	0.22	0.43
Type II SN W95A ($Z_\odot$)[c]	0.24	0.25	0.49
Type II SN W95B ($Z_\odot$)[c]	0.31	0.31	0.46
Type II SN N98S1[d]	0.41	0.61	0.63
Type I SN TNH93[c]	−2.14	−1.44	−0.23
Type I SN WDD2[d]	−2.8	−1.7	0.01
Type I SN W7[d]	−2.18	−1.42	−0.25

Notes. [a]From Savage & Sembach (1996).
[b]From Strickland et al. (2004) Table 10.
[c]IMF-averaged stellar yields from Type I and Type II SNe compiled by Gibson et al. (1997). See Gibson et al. (1997) for model details and nomenclature.
[d]Stellar yields from Type I and Type II SNe from Nagataki & Sato (1998). See Nagataki & Sato (1998) for model details and nomenclature.

Our data do not have the resolution to perform a detail comparison of the emission properties of the numerous smaller clouds within 2″ of the nucleus that were resolved in the *HST* [O III] image (Kristen et al. 1997). However, assuming a temperature of $\sim 10^4$ K and a density of $\sim$100–1000 cm^{-3} for the [O III]-emitting clouds, which are typical values observed in the optical emission-line gas (e.g., Osterbrock & Ferland 2006; Wilson et al. 1985; Ferruit et al. 1999), we estimate the gas pressure of the [O III] clouds to be $\sim 10^{-10}$–10^{-9} dyne cm^{-2}. These pressures are comparable to (or smaller than) the thermal pressure of the hot ISM we calculated in Table 5, implying a possible pressure equilibrium between the X-ray-emitting hot gas and the optical line-emitting cool gas. The X-ray-emitting gas may serve as the hot phase confining intercloud medium to the NLR clouds (see Elvis et al. 1983).

6.2. Hot-Gas Properties and Supernovae Enrichment

As summarized in Section 5.2, the results of our spectral fitting of the diffuse (ENLR cone, diffuse) and of the circumnuclear ring emission (ring), suggest a pervasive hot ISM with temperatures of about 0.6 keV. Metal abundances are overall larger (supersolar) in the ring, and become subsolar at larger radii in the cone region. This temperature and abundance pattern is similar to that of the hot ISM in many regions of NGC 4038/9, "the Antennae" galaxies (see Baldi et al. 2006a, 2006b); not surprisingly, the calculated emission parameters of the hot gas in NGC 1365, such as electron densities, pressure, and cooling times, are also in agreement. In the Antennae, the metal abundances of the hot ISM are consistent with metal enrichment from SN II ejecta. As the ring in NGC 1365 is undergoing a starburst, we may similarly expect to see enhanced abundances.

Nagataki & Sato (1998) show that if the elemental enrichment is from Type II SN ejecta, the expected [Ne/Fe] and [Mg/Fe]

values approach 0.3 and [Si/Fe] approaches 0.5 on average. In contrast, the expected values from Type Ia SN is significantly lower. Thus, we can explore the metal enrichment in NGC 1365 based on this difference. We compiled the element abundances relative to Iron in different regions in Table 5. Together we also show the abundance values from the averaged hot halo of starburst galaxies (Strickland et al. 2004), the warm Galactic halo (Savage & Sembach 1996), and Type Ia, Type II SNe from a variety of theoretical models (Nagataki & Sato 1998). Although there are some uncertainties, the morphologically selected regions in NGC 1365 show [Ne/Fe], [Mg/Fe], and [Si/Fe] ratios fully consistent with a Type II SN-dominated enrichment scenario (see Figure 10). As the circumnuclear ring is where active star formation is occurring and where candidate radio SNe are identified (Galliano et al. 2005), it is plausible that recent episodes of star formation led to the enrichment of the ISM almost exclusively through SNe II injection. Notably the "ring" (and "ring+") region has abundance ratios matching very well with the theoretically predicted values. Two SNe have been seen in NGC 1365 (not related to Galliano et al. radio SNe) in four decades (Lindblad 1999), giving a rate about 6 times higher than our estimated R_{SN} in Table 4 but with a large Poisson error bar. The *HST* optical study by Kristen et al. (1997) estimates a supernovae rate of 10^{-3} yr^{-1} for the luminous star clusters in NGC 1365, which is in good agreement with our derived R_{SN}.

However, we note that these measurements in NGC 1365, similar to X-ray estimates, only place a lower limit on the actual, intrinsic supernova rate as they are severely affected by dust extinction. It is well established that the extinction in LIRGs is high enough to obscure SNe in their central regions, even at near-IR wavelengths (van Buren & Greenhouse 1994; see also the near-IR SN survey by Mannucci et al. 2003). Far-infrared (FIR) studies of starburst galaxies appear to yield a higher SNe explosion rate assuming that L_{FIR} is powered mainly by star formation. Using observations of NGC 253 and M 82, van Buren & Greenhouse (1994) derived the relation $R_{SN} = 2.3 \times 10^{-12}\ L_{FIR}/L_{\odot}$ yr^{-1}. A similar factor ($(2.4 \pm 0.1) \times 10^{-12}$) was derived by Mannucci et al. (2003) and independently (2.7×10^{-12}) by Mattila & Meikle (2001). Applying this to NGC 1365's total L_{FIR} predicts a total SNe rate of $\sim$0.2 yr^{-1}, which is $\sim$20 times higher than the largest diffuse region in Table 4 with $R_{SN} \sim 0.01$ yr^{-1}. Within the ring alone, using our estimate of $\sim$35% of the total L_{FIR} (see Section 6.4) implies $R_{SN} \sim 0.07$ yr^{-1}, which is $\sim$200 times higher than the X-ray estimate in Table 4. This discrepancy can be attributed to a number of uncertainties. First, although we used absorption corrected X-ray luminosity to account for the attenuation of intrinsic X-ray luminosity, this absorption correction derived from spectral fitting is still not precise, especially when the absorption column is high enough to obscure the soft X-rays. In comparison, FIR and radio are known to be reliable quantitative measures of emitted luminosities as most galaxies become transparent at these wavelengths. Second, we estimated R_{SN} assuming that the mechanical energy released in SN explosions heat the ISM thermal emission, the efficiency of which depends on the detailed properties of the interstellar environment. A low efficiency can increase the required R_{SN} by a factor of 100. In addition, the assumed X-ray-emitting volume and volume-filling factor are uncertain and difficult to quantify. Altogether, the X-ray-estimated SN rate should be deemed as a lower limit, and does not contradict the FIR-derived SN rate.

Some caution is warranted as the above analysis relies upon the abundances of the emitting plasma being accurately modeled. Measuring hot-gas elemental abundances through X-ray spectral fitting was recognized to be quite uncertain (especially with the low resolution spectra of CCDs) because of ambiguities in the fits (e.g., a degeneracy between the temperature and metallicity), and strongly dependent on the model choice (see Dahlem et al. 1998; Dahlem et al. 2000; Strickland et al. 2002, 2004; Baldi et al. 2006a). These uncertainties are strongly affected by poor spatial resolution, and spatially resolved spectroscopy is needed to determine reliable constraints. However, the agreement of all the regions on a set of abundances close to the SNe II values seems unlikely to occur by chance and suggest that *Chandra* has spatially resolved the major variations.

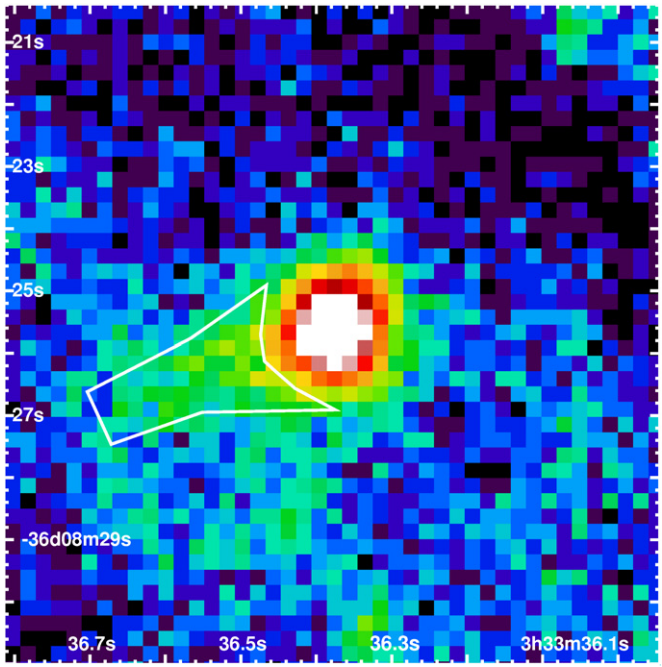

Figure 12. 10″ × 10″ region around the nucleus in the full band (0.3–7 KeV) image (0.″25/pixel binning). A 4″ elongation is seen. A spectrum for the jetlike feature is extracted from the region shown by the white polygon.

(A color version of this figure is available in the online journal.)

6.3. X-ray Emission from the 'jet'

Figure 12 shows that the bright nuclear emission in the full band (0.3–7 keV) shows a clear asymmetry, extending $\sim$ 4″ toward the SE. The orientation of this jetlike feature emanating from the nucleus is well aligned with the cone-axis seen at a larger scale. We consider this to be a candidate X-ray counterpart of the radio jet (NGC 1365:F, radio spectral index −0.94, Sandqvist et al. 1995). However, a fit to the extracted spectra ($\sim$300 net counts) suggests an absorbed power-law emission with $\Gamma \sim 3.9$, which is unusually soft for a jet (Harris & Krawczynski 2006). If the X-rays and radio emission are produced in synchrotron radiation from the same population of electrons, the steep X-ray spectrum implies that the X-ray emission is in the tail of the spectral distribution of the synchrotron radiation ($\nu > \nu_c$, the critical frequency). Alternatively, Stevens et al. (1999) pointed out that the radio feature may represent enhanced star formation often seen at the ends of bars in barred galaxies. This would result in a soft X-ray spectrum similar to the thermal emission from hot gas in the circumnuclear ring, as we see here ($kT \sim 0.8 \pm 0.04$ keV) if we fit the jet spectrum with a single-

Table 6
X-ray and FIR Luminosities of NGC 1365 and Other Starburst Galaxies

Galaxy	$t_{\rm starburst}$ (Myr)[a]	log $N_{\rm H}$ (cm^{-2})[b]	$L_{X,\rm corr}$(ergs s^{-1})[c]	$L_{\rm FIR}$(ergs s^{-1})[d]	$L_{\rm X}/L_{\rm FIR}$	References
NGC 1365	3–6	20.5	5×10^{40}	3.8×10^{44}	1.3×10^{-4}	1,2,3
NGC 1365 Ring	3–6	21.1	2.7×10^{40}	1.4×10^{44}	1.9×10^{-4}	1,4
M82	4–6	21.0	2×10^{40}	9.3×10^{43}	2.2×10^{-4}	5,6,7
NGC 3351	4–5	20.7	3.3×10^{39}	9.5×10^{43}	3.5×10^{-5}	8,9,3
Antennae	4–13	21.2	2×10^{41}	1.4×10^{44}	1.4×10^{-3}	10,11,3
Arp 220	1–3	21.8	2.3×10^{41}	6.8×10^{45}	3.4×10^{-5}	12,13,14
NGC 253	20–30	22.0	6×10^{39}	7×10^{43}	9×10^{-5}	15,16,17
Galactic Center	2–7	22.8	10^{38} :	3.8×10^{42}	3×10^{-5}	18,19

Notes. [a]The age of recent starburst event is taken as the measured range of young star clusters in the starburst galaxy (see Gallagher & Smith 2005 review on difficulties in measuring the ages of starbursts). In the Galactic center, Figer (2008) shows 2–3 Myr for the Arches and the quintuplet clusters, 3–7 Myr for the central cluster.

[b] $N_{\rm H}$ values are taken from X-ray spectral fitting reported in literature if available, otherwise we use $A_{\rm V} \approx 4.5 \times 10^{-22} N_{\rm H}$ (mag) (Ryter 1996) to estimate $N_{\rm H}$. For Arp 220 and NGC 253, we note that both their nuclear starburst regions are heavily obscured with $N_{\rm H} \gtrsim 10^{23}$ cm^{-2}; the values shown here are typical of the more extended regions. Therefore, the absorption-corrected luminosities most likely lower than the intrinsic soft X-ray luminosities.

[c]The absorption corrected soft X-ray luminosity is taken from *ROSAT* results (0.1–2.5 keV) reported in the literature and this work, except for NGC 3351 and the Galactic center. The $L_{\rm X}$ for NGC 3351 is converted from *Chandra* measurement using the best fit model from Swartz et al. (2006). Because of the heavy obscuration, only 2–8 keV measurement is available for the Galactic center and the absorption corrected $L_{X,\rm corr}$ is highly uncertain. For the galaxies with log $N_{\rm H} \sim 21$, the uncertainty in the absorption columns results in a ± 0.08 dex uncertainty in the absorption corrected $L_{X,\rm corr}$ from the XSPEC spectral fit. For Arp 220 and NGC 253, correcting for a log $N_{\rm H} \sim 23$ column (the most obscured nuclear region) can increase $L_{X,\rm corr}$ by a factor of 100. For comparison, we list here X-ray luminosities (0.2–4.0 keV) from Fabbiano et al. (1992) with the *Einstein Observatory* measurements–NGC 1365: log $Lx = 40.84$, M82: log $Lx = 40.56$, NGC 3351: log $Lx < 39.98$, NGC 4038/9: (Antennae) log $Lx = 40.96$, NGC 253: log $Lx = 39.87$, Arp 220: log $Lx = 41.68$.

[d]The FIR luminosities (except that of the NGC 1365 ring) are derived using IRAS measurements (∼10% uncertainty; Ranalli et al. 2003). Helou et al. (1985) gives $FIR = 1.26 \times 10^{-14}(2.58 f_{60\,\mu\rm m} + f_{100\,\mu\rm m})$ W m^{-2}, which is commonly used in the references, where f_ν are the flux densities in Jy. FIR emission from the NGC 1365 ring cannot be accurately measured due to the low spatial resolution at 70 μm and 160 μm (saturated) *Spitzer* images. We estimate $L_{\rm FIR}$ of the ring is ∼35% of the IRAS $L_{\rm FIR}$ for NGC 1365.

References. (1) Galliano et al. (2005, 2008); (2) Stevens et al. (1999); (3) Sanders et al. (2003); (4) This work; (5) Smith et al. (2006); (6) Strickland et al. (1997); (7) Condon et al. (1998); (8) Colina et al. (1997); (9) Swartz et al. (2006); (10) Mengel et al. (2001); (11) Read et al. (1995), see also Fabbiano et al. (1997); (12) Wilson et al. (2006); (13) Heckman et al. (1996), see also McDowell et al. (2003); (14) Soifer et al. (1984); (15) Engelbracht et al. (1998); (16) Weaver et al. (2002); (17) Strickland et al. (2004); (18) Figer (2008) and references therein; (19) Morris & Serabyn (1996); see also Wang et al. (2006); Muno et al. (2004).

temperature thermal emission model. We examined the high angular resolution (0.″07) *HST*/FOC F437M(λ_0 = 4290 Å) image that was presented in Kristen et al. (1997). None of the reported compact continuum source is associated with the jet, with an observed flux completeness limit corresponds to B = 19.3 mag. No apparent mid-IR source is found at the location of the jet in the *Spitzer* IRAC images. The lacking in optical and IR counterparts seems to disfavor the enhanced star formation origin for the X-ray emission. Neither the radio observation nor our X-ray image show evidence for a counter jet. If indeed we are seeing a radio jet, then the observed one-sidedness could be explained by relativistic beaming with a jet velocity 0.7c, or with free–free absorption by the circumnuclear disk as suggested by Hjelm & Lindblad (1996). It is also interesting to note that the X-ray-to-6 cm-luminosity ratio $L_{\rm X}/L_{6\,\rm cm}$ is ∼240 for the jet feature (6 cm luminosity of the jet from Stevens et al. 1999), similar to that of radio SNe and radio quiet quasars (e.g., a few hundred; Stevens et al. 1999; Landt et al. 2001).

6.4. Comparison with Other Galaxies: AGN Feedback versus Starburst Feedback

NGC 1365 is a LIRG ($L_{\rm FIR} = 10^{11}\ L_\odot$; Ghosh et al. 1993; Sanders et al. 2003). The central nucleus contributes little (few percent; Komossa & Schulz 1998) to the total IR luminosity, most of which could be attributed to the active star-forming ring. Sakamoto et al. (2007) found that starburst in subregions of the NGC 1365 circumnuclear ring alone is comparable to the entire starburst in galaxies like M82 and NGC 253. The star formation rate in the inner kpc region is $\Sigma_{\rm SFR} = 3\ M_\odot$ yr^{-1} kpc^{-2}, among the highest in the nonmerging galaxies (Kennicutt 1998).

For star-forming galaxies, a good correlation between the X-ray and the FIR luminosities has long been known and extensively investigated (e.g., Fabbiano et al. 1988; David et al. 1992; Fabbiano & Shapley 2002; Ranalli et al. 2003; Colbert et al. 2004; Persic & Rephaeli 2007). the X-ray emission in the circumnuclear starburst mainly comes from the young SNe (also SNRs) and X-ray binaries (XRBs; Fabbiano 1989), the formation of which requires time for the stellar evolution of O and B stars to complete. Therefore X-ray emission may trace the evolution of a starburst with some delay (a few Myr, the main-sequence life time of a massive star), and the X-ray-to-FIR-luminosity ratio $L_{\rm X}/L_{\rm FIR}$ could reflect the age of the starburst event (see Swartz et al. 2006). Recently Mas-Hesse et al. (2008) computed soft X-ray and FIR luminosities for different starburst scenario (instantaneous or extended), using realistic efficiency of converting mechanical energy into soft X-ray emission, and concluded that the soft X-ray emission can be used to trace the star formation rate in relatively young and unevolved starbursts.

In Table 6, we compiled $L_{\rm X}$ (0.1–2.5 keV; total line-of-sight absorption corrected to represent intrinsic luminosity), IRAS FIR luminosity $L_{\rm FIR}$, and measured ages of young clusters associated with starburst events for a number of starburst galaxies (Condon et al. 1998; Sanders et al. 2003; see complete reference list in the Table 6 footnote). For NGC 1365, we calculated the $L_{\rm X}/L_{\rm FIR}$ using both total (non-nuclear) X-ray emission over total FIR emission, and X-ray emission from circumnuclear starburst ring over FIR emission from the ring. Given the available data, FIR emission from the NGC 1365 ring cannot be accurately measured due to the low spatial resolution at 70 μm and 160 μm (saturated) *Spitzer* images. To derive an approximate $L_{\rm FIR}$ value for the ring, we estimate the $L_{\rm IR}$ ratio

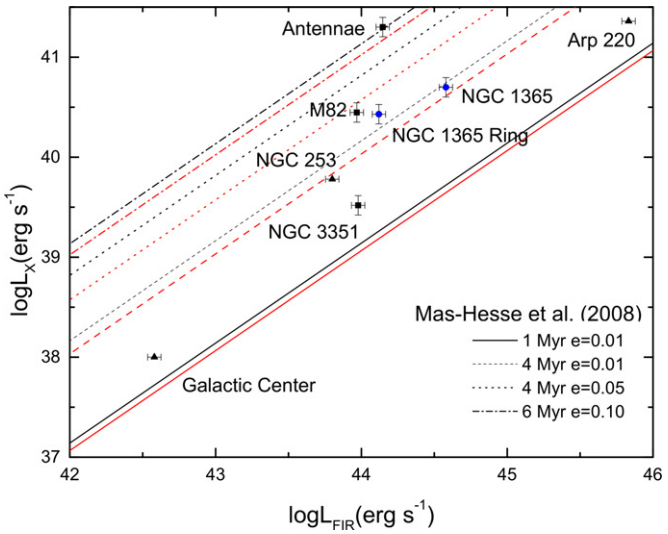

Figure 13. Comparison of the X-ray and FIR luminosities of NGC 1365 and six other galaxies. The predictions of soft X-ray and FIR luminosities from evolutionary synthesis models in Mas-Hesse et al. (2008) are shown as lines (see legend) for different starburst ages, e values (the efficiency of reprocessing mechanical energy into soft X-ray emission, and star formation history: instantaneous starburst (see Mas-Hesse et al. 2008 for detailed model description; all black lines) vs. extended starburst (all red lines). The absorption corrected L_X for NGC 253, Arp 220, and the Galactic Center is considered as lower limit because of the high intrinsic obscuration in these regions. See also Table 6.

(A color version of this figure is available in the online journal.)

between the nucleus and the nucleus combined with the ring at 24 μm, which is ∼50%. Together the nucleus and the ring contribute ∼70% of the FIR emission from NGC 1365, therefore we estimate that $L_{\rm FIR}$ of the ring is approximately 35% of the IRAS $L_{\rm FIR}$ for NGC 1365. The $L_X/L_{\rm FIR} \sim 10^{-4}$ is in good agreement with that of M82, whose $L_X/L_{\rm FIR}$ represents a sample of starburst galaxies (Strickland et al. 2004). In comparison, the ultraluminous IR galaxy (ULIRG) Arp 220 has a lower $L_X/L_{\rm FIR} \sim 3 \times 10^{-5}$ (Soifer et al. 1984; McDowell et al. 2003), which hosts very young clusters (1–3 Myr old; Wilson et al. 2006). On the other hand, the merging system Antennae shows a higher $L_X/L_{\rm FIR}$, where older clusters (age ∼13 Myr) have been found (Mengel et al. 2001). Another well-known starburst galaxy NGC 253 had a starburst event 20–30 Myr ago (Engelbracht et al. 1998). Its $L_X/L_{\rm FIR} \sim 10^{-4}$ is a lower limit because of the high obscuration of soft X-ray emission in the starburst nucleus, which could be similar to that of the Antennae. We also included the Galactic center, if viewed from outside of our Galaxy, the Galactic center will appear as a circumnuclear starburst with a weakly active nucleus (Sgr A*).

Figure 13 shows the resulting L_X versus $L_{\rm FIR}$ plot and the predicted values for 1 Myr, 4 Myr, and 6 Myr old starbursts from Mas-Hesse et al. (2008). The different assumptions on star formation history and energy conversion efficiency yield similar predictions for such relatively unevolved systems. Their locations relative to the model tracks show that the starburst in NGC 3351 is over 1 Myr old. NGC 1365, M82, and NGC 253 lie closely with the 4 Myr model tracks, and the older merging system Antennae shows values consistent with the 6 Myr model. Comparing to the ages obtained in the literature (see Table 6), these values derived from the model tracks appear to be qualitatively consistent but a few Myrs younger. Many factors may contribute to this: the assumption of the star formation history in the galaxies is apparently oversimplified; the predicted age in the model is coupled with the efficiency of reprocessing mechanical energy into soft X-ray emission, which could vary in different ISM environment; the measured values from literature also have large range as charting the age of starbursts is challenging (see Gallagher & Smith 2005 review); the measured soft band L_X can be significantly underestimated because of the heavily obscured starburst regions (see related discussion in Table 6 footnotes). This raises caution that the comparison with theoretical evolution may only be used to roughly estimate the age of starbursts.

It is known that the emergent soft X-ray luminosities may be greatly reduced from the star-forming galaxies with significant visual extinction.[13] However, accurate attenuation corrections are unrealistic, the intrinsic absorption columns toward the galaxies are inhomogeneous and difficult to measure. For example, the extinction to the core of Arp 220 is estimated at $A_V > 100$ mag from submillimeter continuum measurements (Sakamoto et al. 2008), while the revealed star clusters have $A_V \sim 3$ mag (Wilson et al. 2006). To correct for absorption, we adopt N_H from X-ray spectral fit if available, otherwise we convert published A_V that are typical of the star clusters to N_H using the Galactic gas-to-dust ratio. For the galaxies with $\log N_H \sim 21$, the uncertainty in the absorption columns results in a ±0.08 dex uncertainty in the absorption corrected $L_{X,\rm corr}$ from the XSPEC spectral fit. For Arp 220 and NGC 253, correcting for a $\log N_H \sim 23$ column (the most obscured nuclear region) can increase $L_{X,\rm corr}$ by a factor of 100 (see Lutz et al. 2004 for estimated correction in Type 2 Seyferts). In comparison, the correlation between the X-ray luminosities (0.5–4.5 keV band) and the FIR luminosities derived in David et al. (1992) assumes an average $N_H = 3 \times 10^{20}$ cm^{-2} for all FIR bright galaxies; the empirical calibration between the soft X-ray luminosities (0.5–2.0 keV) and the FIR luminosities in Ranalli et al. (2003) is corrected for Galactic absorption only.

Swartz et al. (2006) reported *Chandra* observations of the nearby ($D = 10$ Mpc) barred spiral galaxy, NGC 3351, which has a prominent kpc wide circumnuclear ring in reminiscent of the NGC 1365 ring. The X-ray emission in the NGC 3351 ring has $kT \sim 0.5$ keV ($L_X \sim 6.5 \times 10^{38}$ ergs s^{-1}, 0.3–3.0 keV), attributed to hot diffuse gas associated with starburst. The X-ray luminosity of the central nucleus is estimated to be $Lx < 10^{37}$ ergs s^{-1} (0.5–8.0 keV), and X-ray photoionization is considered unimportant. The extended soft X-ray emission, similar to what we see in NGC 1365, is interpreted as gas outflow from the star-forming ring out of the galactic plane.

A multiwavelength study of the circumnuclear extended emission in Seyfert 2 galaxy NGC 2110 (Evans et al. 2006) suggested that shock-heated multiphase gas can account for the observations, although photoionized gas by the nucleus cannot be ruled out. In contrast, in another nearby AGN-starburst galaxy NGC 6764, Croston et al. (2008) detected extended, $kT = 0.75$ keV X-ray emission coincident with the radio bubbles, likely inflated by the AGN (Hota & Saikia 2006). They ruled out a galactic wind as the origin of the X-ray emission and instead favored hot gas heated by jet/ISM interaction in the AGN outflow, similar to the radio lobes in radio galaxies (e.g., Centaurus A, Kraft et al. 2003). This is quite a different situation from NGC 1365, which shows a weak radio nucleus and jet, and no radio bubble (Sandqvist et al. 1995).

Comparison of NGC 1365 to these starburst and Seyfert 2 galaxies suggests that, in galaxies where the AGN is not the

[13] Combining $A_V \approx 4.5 \times 10^{-22} N_H$ (mag) (Ryter 1996) with the X-ray absorption cross sections from Morrison & McCammon (1983) gives $\tau_X \gtrsim 1$ at $E \approx 2$ keV, when $A_V \gtrsim 10$.

dominant energetic factor in the circumnuclear environment (i.e., where a starburst plays major role), the extended soft X-ray emission shows a thermal origin as SNe, and massive stars drive outflow into the disk and halo (galactic winds, see Heckman et al. 1990; Heckman 2001; Strickland et al. 2004). If instead the energetics of nuclear radiation suffice, circumnuclear X-ray emission may be solely attributed to AGN photoionization (e.g., Ogle et al. 2003; Bianchi et al. 2006). When a powerful AGN jet/outflow is seen as evidenced by large-scale radio bubbles, the interaction with the ISM may heat the entrained gas and account for the X-ray emission (e.g., Kraft et al. 2003; Croston et al. 2008). These galaxy feedback processes are critical in our understanding of galaxy formation and evolution, which can be best studied when high resolution radio, X-ray, and optical NLR data are combined (e.g., Evans et al. 2006; Bianchi et al. 2007).

7. SUMMARY

We have presented a detailed *Chandra*/ACIS imaging study of the nearby Seyfert galaxy NGC 1365. Based on the high resolution 100 ks images, we confirm results from previous X-ray studies and present new findings in the complex circumnuclear region.

We have created an X-ray broadband color image as well as narrow bandline-emission image, showing a biconical soft X-ray-emission region extending from the nucleus, coincident with the high-excitation outflow cones seen in [O III]/Hα-emission-line images. A prominent kpc-scale circumnuclear star-forming ring is seen emitting harder X-rays. The spectral fitting on the spatially separated components indicates a thermal plasma origin for the X-ray emission in the ionization cones, which is also supported by the spatial anticorrelation between X-ray emission and the [O III] emission. The abundance ratios for regions of NGC 1365 are fully consistent with the theoretical values for enrichment from Type II SNe. X-ray morphology of NGC 1365 is compared with *Spitzer* mid-IR images and [O III]-emission-line observations. We argue that pure photoionization by AGN cannot account for the extended soft X-ray emission based on the spectral fit, energetic estimate, and morphology evidences. We attribute the observed soft X-rays to thermal emission from shock-heated hot gas, although we cannot rule out a photoionized contribution in the line emission. X-ray emission from a previously reported nuclear radio jet is detected.

Further progress will require deeper *Chandra* images of NGC 1365, which we plan to obtain in the future to enable studies of the morphology and spectral properties in greater details (similar to Baldi et al. 2006a, 2006b), with better statistics and constraints. Isolation of discrete sources in the deep images will allow removal of contribution from the XRB population to the diffuse emission. This enables investigations to distinguish the nature of X-ray hot spots from the truly diffuse emission they embedded in, and studies of the X-ray-luminosity function of XRBs in NGC 1365. Spatial complexity of the X-ray emission can be overcome by dividing the circumnuclear ring and diffuse cones to smaller regions. This will also localize any abundance anomalies. With more counts in the diffuse emission, we will be able to perform spectral modeling on the radial gradient with different models and search for variation in the X-ray structure and spectra. Expecting that a photoionized wind will have constant ionization parameter, and that a thermal wind will cool radially, we plan to use this diagnostic to unambiguously test the photoionized wind model and thermal wind model for the origin of X-ray emission associated with the ENLR in NGC 1365. Radially constant ionization parameters have been found in a sample of Type 2 Seyferts (Bianchi et al. 2006), suggesting that at least in some cases, soft X-ray and optical NLR come from a single photoionized medium. Deeper X-ray imaging will also clarify the nature of the jetlike feature.

We thank an anonymous referee for helpful comments that improved the clarity of the manuscript. We are grateful to S. Veilleux for providing us the [O III] images in Veilleux et al. (2003), and Tim Kallman for the helpful information about XSTAR. J.W. thanks A. Baldi for his help in the data analysis, H. Oti Floranes for providing the model results in Mas-Hesse et al. (2008), and A. Siemiginowska for helpful discussion on radio jets. G.F. and M.E. acknowledge stimulating discussions at the Aspen Center for Physics workshop on Active Galactic Nuclei. This work is supported by NASA Contract NAS8-39073 (CXC) and *Chandra* GO Grant G06-7102X (PI: Risaliti).

REFERENCES

Anders, E., & Grevesse, N. 1989, Geochim. Cosmochim. Acta, 53, 197
Arnaud, K. A. 1996, Astronomical Data Analysis Software and Systems V, 101, 17
Baldi, A., Raymond, J. C., Fabbiano, G., Zezas, A., Rots, A. H., Schweizer, F., King, A. R., & Ponman, T. J. 2006a, ApJ, 636, 158
Baldi, A., Raymond, J. C., Fabbiano, G., Zezas, A., Rots, A. H., Schweizer, F., King, A. R., & Ponman, T. J. 2006b, ApJS, 162, 113
Bianchi, S., Guainazzi, M., & Chiaberge, M. 2006, A&A, 448, 499
Bianchi, S., Chiaberge, M., Piconcelli, E., & Guainazzi, M. 2007, MNRAS, 374, 697
Burbidge, E. M., & Burbidge, G. R. 1960, ApJ, 132, 30
Colbert, E. J. M., Heckman, T. M., Ptak, A. F., Strickland, D. K., & Weaver, K. A. 2004, ApJ, 602, 231
Colina, L., Garcia Vargas, M. L., Mas-Hesse, J. M., Alberdi, A., & Krabbe, A. 1997, ApJ, 484, L41
Condon, J. J., Yin, Q. F., Thuan, T. X., & Boller, T. 1998, AJ, 116, 2682
Croston, J. H., Hardcastle, M. J., Kharb, P., Kraft, R. P., & Hota, A. 2008, ApJ, 688, 190
Dahlem, M., Parmar, A., Oosterbroek, T., Orr, A., Weaver, K. A., & Heckman, T. M. 2000, ApJ, 538, 555
Dahlem, M., Weaver, K. A., & Heckman, T. M. 1998, ApJS, 118, 401
David, L. P., Jones, C., & Forman, W. 1992, ApJ, 388, 82
Elvis, M., Briel, U. G., & Henry, J. P. 1983, ApJ, 268, 105
Elmegreen, B. G. 1994, ApJ, 425, L73
Engelbracht, C. W., Rieke, M. J., Rieke, G. H., Kelly, D. M., & Achtermann, J. M. 1998, ApJ, 505, 639
Evans, D. A., Lee, J. C., Kamenetska, M., Gallagher, S. C., Kraft, R. P., Hardcastle, M. J., & Weaver, K. A. 2006, ApJ, 653, 1121
Evans, D. A., Lee, J. C., Turner, T. J., Weaver, K. A., & Marshall, H. L. 2007, ApJ, 671, 1345
Fabbiano, G. 1989, ARA&A, 27, 87
Fabbiano, G., Gioia, I. M., & Trinchieri, G. 1988, ApJ, 324, 749
Fabbiano, G., Kim, D.-W., & Trinchieri, G. 1992, ApJS, 80, 531
Fabbiano, G., Krauss, M., Zezas, A., Rots, A., & Neff, S. 2003, ApJ, 598, 272
Fabbiano, G., Schweizer, F., & Mackie, G. 1997, ApJ, 478, 542
Fabbiano, G., & Shapley, A. 2002, ApJ, 565, 908
Fabbiano, G., et al. 2004, ApJ, 605, L21
Fazio, G. G., et al. 2004, ApJS, 154, 10
Ferruit, P., Wilson, A. S., Whittle, M., Simpson, C., Mulchaey, J. S., & Ferland, G. J. 1999, ApJ, 523, 147
Figer, D. F. 2008, arXiv:0803.1619
Forbes, D. A., & Norris, R. P. 1998, MNRAS, 300, 757
Freeman, P. E., Kashyap, V., Rosner, R., & Lamb, D. Q. 2002, ApJS, 138, 185
Gallagher, J. S., & Smith, L. J. 2005, AIP Conf. Proc. 783, The Evolution of Starbursts (New York: AIP), 271
Galliano, E., Alloin, D., Pantin, E., Granato, G. L., Delva, P., Silva, L., Lagage, P. O., & Panuzzo, P. 2008, A&A, 492, 3
Galliano, E., Alloin, D., Pantin, E., Lagage, P. O., & Marco, O. 2005, A&A, 438, 803
Garmire, G. P., Bautz, M. W., Ford, P. G., Nousek, J. A., & Ricker, G. R., Jr. 2003, Proc. SPIE, 4851, 28
Ghosh, S. K., Verma, R. P., Rengarajan, T. N., Das, B., & Saraiya, H. T. 1993, ApJS, 86, 401
Gibson, B. K., Loewenstein, M., & Mushotzky, R. F. 1997, MNRAS, 290, 623

González Delgado, R. M., Heckman, T., Leitherer, C., Meurer, G., Krolik, J., Wilson, A. S., Kinney, A., & Koratkar, A. 1998, ApJ, 505, 174
Guainazzi, M., & Bianchi, S. 2007, MNRAS, 374, 1290
Harris, D. E., & Krawczynski, H. 2006, ARA&A, 44, 463
Heckman, T. M. 2001, ASP Conf. Proc. 240, Gas and Galaxy Evolution, ed. J. E. Hibbard, M. Rupen, & J. H. van Gorkom (San Francisco, CA: ASP), 345
Heckman, T. M., Armus, L., & Miley, G. K. 1990, ApJS, 74, 833
Heckman, T. M., Dahlem, M., Eales, S. A., Fabbiano, G., & Weaver, K. 1996, ApJ, 457, 616
Helou, G., Soifer, B. T., & Rowan-Robinson, M. 1985, ApJ, 298, L7
Hjelm, M., & Lindblad, P. O. 1996, A&A, 305, 727
Hopkins, P. F., Somerville, R. S., Hernquist, L., Cox, T. J., Robertson, B., & Li, Y. 2006, ApJ, 652, 864
Hota, A., & Saikia, D. J. 2006, MNRAS, 371, 945
Iyomoto, N., Makishima, K., Fukazawa, Y., Tashiro, M., & Ishisaki, Y. 1997, PASJ, 49, 425
Jones, J. E., & Jones, B. J. T. 1980, MNRAS, 191, 685
Kauffmann, G., et al. 2003, MNRAS, 346, 1055
Kalberla, P. M. W., Burton, W. B., Hartmann, D., Arnal, E. M., Bajaja, E., Morras, R., & Pöppel, W. G. L. 2005, A&A, 440, 775
Kallman, T., & Bautista, M. 2001, ApJS, 133, 221
Kallman, T. R., & McCray, R. 1982, ApJS, 50, 263
Kennicutt, R. C., Jr. 1998, ARA&A, 36, 189
Komossa, S., & Schulz, H. 1998, A&A, 339, 345
Kraemer, S. B., Schmitt, H. R., & Crenshaw, D. M. 2008, ApJ, 679, 1128
Kraft, R. P., Vázquez, S. E., Forman, W. R., Jones, C., Murray, S. S., Hardcastle, M. J., Worrall, D. M., & Churazov, E. 2003, ApJ, 592, 129
Kristen, H., Jorsater, S., Lindblad, P. O., & Boksenberg, A. 1997, A&A, 328, 483
Landt, H., Padovani, P., Perlman, E. S., Giommi, P., Bignall, H., & Tzioumis, A. 2001, MNRAS, 323, 757
Lindblad, P. A. B., Lindblad, P. O., & Athanassoula, E. 1996, A&A, 313, 65
Lindblad, P. O. 1999, A&AR, 9, 221
Longinotti, A. L., Bianchi, S., Santos-Lleo, M., Rodríguez-Pascual, P., Guainazzi, M., Cardaci, M., & Pollock, A. M. T. 2007, A&A, 470, 73
Lutz, D., Maiolino, R., Spoon, H. W. W., & Moorwood, A. F. M. 2004, A&A, 418, 465
Madore, B. F., et al. 1998, Nature, 395, 47
Madore, B. F., et al. 1999, ApJ, 515, 29
Maiolino, R., & Rieke, G. H. 1995, ApJ, 454, 95
Maiolino, R., Marconi, A., Salvati, M., Risaliti, G., Severgnini, P., Oliva, E., La Franca, F., & Vanzi, L. 2001, A&A, 365, 28
Mannucci, F., et al. 2003, A&A, 401, 519
Mas-Hesse, J. M., Otí-Floranes, H., & Cerviño, M. 2008, A&A, 483, 71
Mason, K. O., et al. 2001, A&A, 365, L36
Mattila, S., & Meikle, W. P. S. 2001, MNRAS, 324, 325
McDowell, J. C., et al. 2003, ApJ, 591, 154
Mengel, S., Lehnert, M. D., Thatte, N., Tacconi-Garman, L. E., & Genzel, R. 2001, ApJ, 550, 280
Morris, M., & Serabyn, E. 1996, ARA&A, 34, 645
Morrison, R., & McCammon, D. 1983, ApJ, 270, 119
Muno, M. P., et al. 2004, ApJ, 613, 326
Nagataki, S., & Sato, K. 1998, ApJ, 504, 629
Ogle, P. M., Brookings, T., Canizares, C. R., Lee, J. C., & Marshall, H. L. 2003, A&A, 402, 849
Ogle, P. M., Marshall, H. L., Lee, J. C., & Canizares, C. R. 2000, ApJ, 545, L81
Osterbrock, D. E., & Ferland, G. J. 2006, Astrophysics of Gaseous Nebulae and Active Galactic Nuclei (2nd ed.; Sausalito, CA: Univ. Science Books)
Persic, M., & Rephaeli, Y. 2007, A&A, 463, 481
Phillips, K. J. H., et al. 1982, ApJ, 256, 774
Phillips, M. M., Edmunds, M. G., Pagel, B. E. J., & Turtle, A. J. 1983, MNRAS, 203, 759
Ranalli, P., Comastri, A., & Setti, G. 2003, A&A, 399, 39
Read, A. M., Ponman, T. J., & Wolstencroft, R. D. 1995, MNRAS, 277, 397
Risaliti, G., Bianchi, S., Matt, G., Baldi, A., Elvis, M., Fabbiano, G., & Zezas, A. 2005a, ApJ, 630, L129
Risaliti, G., Elvis, M., Fabbiano, G., Baldi, A., & Zezas, A. 2005b, ApJ, 623, L93
Risaliti, G., Elvis, M., Fabbiano, G., Baldi, A., Zezas, A., & Salvati, M. 2007, ApJ, 659, L111
Roy, J.-R., & Walsh, J. R. 1997, MNRAS, 288, 715
Ryter, C. E. 1996, APSS, 236, 285
Sakamoto, K., Ho, P. T. P., Mao, R.-Q., Matsushita, S., & Peck, A. B. 2007, ApJ, 654, 782
Sakamoto, K., et al. 2008, ApJ, 684, 957
Sandage, A., & Tammann, G. A. 1981, A revised Shapley-Ames Catalog of Bright Galaxies (Washington: Carnegie Institution)
Sanders, D. B., Mazzarella, J. M., Kim, D.-C., Surace, J. A., & Soifer, B. T. 2003, AJ, 126, 1607
Sandqvist, A. 1999, A&A, 343, 367
Sandqvist, A., Joersaeter, S., & Lindblad, P. O. 1995, A&A, 295, 585
Savage, B. D., & Sembach, K. R. 1996, ARA&A, 34, 279
Sazonov, S. Y., Ostriker, J. P., & Sunyaev, R. A. 2004, MNRAS, 347, 144
Schmitt, H. R., Donley, J. L., Antonucci, R. R. J., Hutchings, J. B., & Kinney, A. L. 2003, ApJS, 148, 327
Schulz, H., Komossa, S., Schmitz, C., & Mücke, A. 1999, A&A, 346, 764
Scoville, N. Z. 1992, ASP Conf. Ser. 31, Relationships Between Active Galactic Nuclei and Starburst Galaxies, ed. A. V. Filippenko (San Francisco, CA: ASP), 159
Sérsic, J. L., & Pastoriza, M. 1965, PASP, 77, 287
Silbermann, N. A., et al. 1999, ApJ, 515, 1
Silk, J., & Rees, M. J. 1998, A&A, 331, L1
Smith, L. J., Westmoquette, M. S., Gallagher, J. S., O'Connell, R. W., Rosario, D. J., & de Grijs, R. 2006, MNRAS, 370, 513
Smith, R. K., Brickhouse, N. S., Liedahl, D. A., & Raymond, J. C. 2001, ApJ, 556, L91
Soifer, B. T., et al. 1984, ApJ, 283, L1
Soria, R., Baldi, A., Risaliti, G., Fabbiano, G., King, A., La Parola, V., & Zezas, A. 2007, MNRAS, 379, 1313
Stevens, I. R., Forbes, D. A., & Norris, R. P. 1999, MNRAS, 306, 479
Storchi-Bergmann, T., & Bonatto, C. J. 1991, MNRAS, 250, 138
Strateva, I. V., & Komossa, S. 2009, ApJ, 692, 443
Strickland, D. K., Heckman, T. M., Colbert, E. J. M., Hoopes, C. G., & Weaver, K. A. 2004, ApJS, 151, 193
Strickland, D. K., Heckman, T. M., Weaver, K. A., Hoopes, C. G., & Dahlem, M. 2002, ApJ, 568, 689
Strickland, D. K., Ponman, T. J., & Stevens, I. R. 1997, A&A, 320, 378
Swartz, D. A., Yukita, M., Tennant, A. F., Soria, R., & Ghosh, K. K. 2006, ApJ, 647, 1030
Tucker, W. 1975, Radiation Processes in Astrophysics (Cambridge, MA: MIT Press)
Turner, T. J., Urry, C. M., & Mushotzky, R. F. 1993, ApJ, 418, 653
Tyler, K., Quillen, A. C., LaPage, A., & Rieke, G. H. 2004, ApJ, 610, 213
van Buren, D., & Greenhouse, M. A. 1994, ApJ, 431, 640
van Speybroeck, L. P., Jerius, D., Edgar, R. J., Gaetz, T. J., Zhao, P., & Reid, P. B. 1997, Proc. SPIE, 3113, 89
Veilleux, S., Kim, D.-C., Sanders, D. B., Mazzarella, J. M., & Soifer, B. T. 1995, ApJS, 98, 171
Veilleux, S. 2001, in Proc. Workshop, Starburst Galaxies: Near and Far (Ringberg Castle, Germany, 2000 September 10–15), ed. L. Tacconi & D. Lutz (Heidelberg: Springer), 88
Veilleux, S., Shopbell, P. L., Rupke, D. S., Bland-Hawthorn, J., & Cecil, G. 2003, AJ, 126, 2185
Veron, P., Lindblad, P. O., Zuiderwijk, E. J., Veron, M. P., & Adam, G. 1980, A&A, 87, 245
Wang, J. M., Chen, Y. M., Yan, C. S., Hu, C., & Bian, W. H. 2007, ApJ, 661, L143
Wang, Q. D., Dong, H., & Lang, C. 2006, MNRAS, 371, 38
Warwick, R. S., Jenkins, L. P., Read, A. M., Roberts, T. P., & Owen, R. A. 2007, MNRAS, 376, 1611
Weaver, K. A., Mushotzky, R. F., Serlemitsos, P. J., Wilson, A. S., Elvis, M., & Briel, U. 1995, ApJ, 442, 597
Weaver, K. A., Heckman, T. M., Strickland, D. K., & Dahlem, M. 2002, ApJ, 576, L19
Weisskopf, M. C., Brinkman, B., Canizares, C., Garmire, G., Murray, S., & Van Speybroeck, L. P. 2002, PASP, 114, 1
Werner, M. W., et al. 2004, ApJS, 154, 1
Wilms, J., Allen, A., & McCray, R. 2000, ApJ, 542, 914
Wilson, A. S., Baldwin, J. A., & Ulvestad, J. S. 1985, ApJ, 291, 627
Wilson, C. D., Harris, W. E., Longden, R., & Scoville, N. Z. 2006, ApJ, 641, 763
Yang, Y., Wilson, A. S., & Ferruit, P. 2001, ApJ, 563, 124
Young, A. J., Wilson, A. S., & Shopbell, P. L. 2001, ApJ, 556, 6
Zacharias, N., Monet, D. G., Levine, S. E., Urban, S. E., Gaume, R., & Wycoff, G. L. 2004, Bull. Am. Astron. Soc., 36, 1418